Structural basis for Mg^{2+}-dependent autoinhibition and stepwise gating in the *Arabidopsis* MRS2-1 Mg^{2+} channel

Hexin Xu[1, 7], Chang-Yan Shao[2, 7], Yinglan Wang[3, 7], Xinyu Teng[1], Cheng Shen[1], Zhixuan Zhao[1], Fei Jin[1], Yichen Huang[1], Yimeng Zhao[1], Go Kasuya[4], Natsuko I Kobayashi[5], Keitaro Tanoi[5], Jun-Li Hou[3], Wenning Wang[3], Ye Yu[2, 6], Meng-Yang Sun[2, *], Motoyuki Hattori[1, *]

Affiliations

[1]*State Key Laboratory of Genetics and Development of Complex Phenotypes, Collaborative Innovation Center of Genetics and Development, Department of Physiology and Neurobiology, School of Life Sciences, Fudan University, Shanghai 200438, China;*

[2]*State Key Laboratory of Natural Medicines, School of Basic Medicine and Clinical Pharmacy, China Pharmaceutical University, Nanjing 200098, China;*

[3]*Department of Chemistry, Institute of Biomedical Sciences and Multiscale Research Institute of Complex Systems, Fudan University, Shanghai 200438, China;*

[4]*Division of Integrative Physiology, Department of Physiology, Jichi Medical University, 3311-1 Yakushiji, Shimotsuke, Tochigi, 329-0498, Japan;*

[5]*Graduate School of Agricultural and Life Sciences, The University of Tokyo, 1-1-1 Yayoi, Bunkyo-ku, Tokyo 113-8657, Japan;*

[6]*School of Life Sciences and Key Laboratory of Preclinical Study for New Drugs of Gansu Province, School of Basic Medical Sciences, Lanzhou University, Lanzhou 730000, China.*

[7]*These authors contributed equally: Hexin Xu, Chang-Yan Shao, Yinglan Wang*

[*]Email: mengyangsun@cpu.edu.cn; hattorim@fudan.edu.cn

Author contributions: M.S. and M.H. designed research; H.X., CY.S., Y.W., X.T., C.S., Z.Z., F.J., Y.H., Y.Z., G.K., N.I.K. and K.T. performed research; H.X., CY.S., Y.W., JL.H., W.W., Y.Y., M.S., and M.H. analyzed data; H.X., CY.S., Y.W., Y.Y., M.S., and M.H. wrote the paper.

Competing Interest Statement: The authors declare no competing interest.

Classification: Biological Sciences/Biophysics and Computational Biology

Keywords: ion channels, cryo-EM, patch clamp

Abstract

Magnesium ion (Mg^{2+}) is essential for plant growth and metabolism, and plant MRS2/MGT channels, which belong to the diverse metal ion transporter (MIT) superfamily, mediate Mg^{2+} transport for Mg^{2+} homeostasis, yet the structural basis of Mg^{2+} transport by plant MRS2/MGT channels remains poorly understood. Here, we determined cryo-EM structures of *Arabidopsis thaliana* MRS2-1 (AtMRS2-1) in the presence and absence of Mg^{2+}, together with whole-cell patch-clamp recordings and molecular dynamics simulations to investigate its gating mechanism. In the Mg^{2+}-bound structure, AtMRS2-1 adopts a closed conformation with multiple cytoplasmic Mg^{2+}-binding sites. These sites are distinct from those reported in other bacterial and eukaryotic MIT-superfamily members, indicating divergence in cytoplasmic Mg^{2+} sensing within the MIT superfamily. Patch-clamp recordings showed that these cytoplasmic sites contribute to cytoplasmic Mg^{2+}-dependent autoinhibition. Under Mg^{2+}-free conditions, AtMRS2-1 adopts two distinct conformations. State II exhibits an expanded pore and likely corresponds to the open state. By contrast, State I displays partial expansion of the cytoplasmic domain while the pore remains closed, suggesting an intermediate state along the activation pathway. In State I, Arg225 in one subunit

interacts with Tyr354 and Thr358 in the adjacent subunit, and disruption of these interactions impairs channel activity. Together, our results support a stepwise gating model in which dissociation of cytoplasmic Mg^{2+} drives cytoplasmic-domain rearrangement, leading to an intermediate state consistent with a preopen state before full pore opening. These findings provide a structural framework for Mg^{2+} sensing, autoinhibition, and stepwise gating in a plant MRS2 channel, while extending the comparative framework for MIT-superfamily gating mechanisms.

Significance Statement

Plant MRS2/MGT channels belong to the MIT superfamily and are essential for Mg^{2+} homeostasis, yet no experimentally determined structure of a plant MRS2 channel has been available. We determined cryo-EM structures of Arabidopsis thaliana MRS2-1 in the presence and absence of Mg^{2+}. AtMRS2-1 has cytoplasmic Mg^{2+}-binding sites conserved among *Arabidopsis* MRS2 proteins but distinct from those of bacterial and eukaryotic members of the MIT superfamily, defining a plant-specific mode of cytoplasmic Mg^{2+} sensing. We also captured an open state and a likely preopen intermediate state, supporting a stepwise gating mechanism in plant MRS2. Together, these findings establish a structural framework for a plant MRS2 channel and broaden our understanding of Mg^{2+} sensing and gating in the MIT superfamily.

Introduction

The magnesium ion (Mg^{2+}) is one of the most abundant divalent cations and is indispensable for all domains of life (1, 2). Mg^{2+} mediates fundamental biochemical processes that are conserved across organisms, such as the stabilization of ribosomes and the genome, as well as numerous

68 enzymatic reactions (3, 4). In plants, Mg^{2+} is the central cofactor of chlorophyll and is therefore
69 essential for light harvesting and photosynthetic energy conversion (5). Mg^{2+} availability in plants
70 affects CO_2 assimilation, protein synthesis, and carbohydrate metabolism and allocation (6, 7). Thus,
71 disruption of Mg^{2+} homeostasis causes broad physiological defects, including interveinal chlorosis
72 in older leaves, impaired photosynthesis, abnormal accumulation of sugars and starch, and reduced
73 plant growth and productivity (8).

74 The metal ion transporter (MIT) superfamily includes key players in Mg^{2+} homeostasis
75 throughout evolution, although their physiological roles have diversified in different kingdoms (9).
76 In bacterial members of the MIT superfamily, the CorA Mg^{2+} channel is a widely conserved major
77 Mg^{2+} uptake system (10), and has attracted attention as a target for anti-virulence drugs (11-13). In
78 mammals, the CorA orthologue MRS2 is a mitochondrial Mg^{2+} channel that mediates Mg^{2+} influx
79 into the matrix and is required for normal mitochondrial function (14). In addition, MRS2 has been
80 implicated in multidrug resistance in gastric cancer cells (15), and MRS2 dysfunction has been
81 associated with demyelination (16).

82 In plants, the MRS2 family, also known as MGT, has expanded to coordinate Mg^{2+} uptake,
83 intracellular partitioning, and organellar Mg^{2+} homeostasis in highly compartmentalized
84 photosynthetic cells (17-19). For instance, *Arabidopsis thaliana* contains nine annotated
85 MRS2/MGT genes (AtMRS2) and two pseudogenes, and the family is often referred to as having
86 10 members in earlier literature (18, 19). AtMRS2-1/MGT2 and AtMRS2-10/MGT1 are important
87 for plant growth under low-Mg^{2+} conditions (20, 21). AtMRS2-4/MGT6 mediates root Mg^{2+} uptake
88 under Mg limitation, whereas AtMRS2-11/MGT10 is required for chloroplast development and
89 photosynthesis (22, 23).

Structurally, Mg^{2+} channels in the MIT superfamily have been characterized mainly through studies of bacterial CorA, particularly *Thermotoga maritima* CorA (TmCorA) (24-27), and more recently through studies of eukaryotic MRS2 (28-31). Biophysical studies have shown that CorA is negatively regulated by intracellular Mg^{2+}, and that Mg^{2+}-dependent structural changes in the cytoplasmic domain are associated with channel gating for Mg^{2+} homeostasis (32, 33). Recent structural analyses of human MRS2 (hMRS2) showed that the eukaryotic homolog preserves essentially the same pentameric architecture but that its cytoplasmic divalent cation-binding sites differ from those of bacterial CorA (28-30). Furthermore, cryo-EM analyses of fungal MRS2 (*Chaetomium thermophilum* MRS2, CtMRS2) in the Mg^{2+}-bound and Mg^{2+}-free states revealed a symmetric channel opening mechanism (31), which also differs from bacterial CorA, where asymmetric structural changes were reported under Mg^{2+}-free conditions (34). Thus, structural analyses of CorA and MRS2 to date suggest that, even among Mg^{2+} channels within the same MIT superfamily, there is diversity in the cytoplasmic regulatory metal-binding sites and in the channel gating mechanisms. Accordingly, Mg^{2+} recognition, channel gating, and regulatory mechanisms of plant MRS2 proteins may also have diverged, particularly given their limited overall sequence conservation with bacterial CorA and other eukaryotic MRS2 homologs. However, despite the important physiological roles assigned to plant MRS2 proteins, their molecular mechanisms of Mg^{2+} transport remain poorly understood because no experimentally determined structure of a plant MRS2 channel has been reported.

Here, we report the cryo-EM structures of *Arabidopsis thaliana* MRS2-1 in the presence and absence of Mg^{2+} ions, along with structure-based functional analyses and molecular dynamics (MD) simulations. Our work provides structural insights into Mg^{2+} permeation, gating, and regulation of

plant MRS2, highlighting mechanistic features that are distinct from those of bacterial CorA and other eukaryotic MRS2 homologs.

Results

Structure determination and functional characterization

Our expression screening of *Arabidopsis thaliana* MRS2 proteins by fluorescence-detection size-exclusion chromatography (FSEC) (35) and FSEC-based thermostability assays (FSEC-TS) identified *Arabidopsis thaliana* MRS2-1 (AtMRS2-1) as a suitable candidate for structural studies. Further optimization of the construct and detergent conditions showed that truncation of the N-terminal disordered 43 residues (AtMRS2-1 ΔN43), together with the use of GDN, yielded a sharp peak in size-exclusion chromatography (**Fig. S1A**). To assess the functionality of this AtMRS2-1 construct, we performed whole-cell patch-clamp recordings. Upon application of an external solution containing 20 mM $MgCl_2$, we observed inward currents specifically in cells expressing the AtMRS2-1 construct (**Figs. S1B-S1D**), suggesting that the construct is functional and mediates Mg^{2+} currents.

We then employed single-particle cryogenic electron microscopy (cryo-EM) to determine the structure of AtMRS2-1 in the presence of Mg^{2+} ions (**Figs. S2 and S3**). 3D reconstruction yielded a cryo-EM density map at an overall resolution of 2.44 Å (**Figs. S2 and S3**). Although part of a loop region in the cytoplasmic domain (residues 144-170) was disordered, we were able to build a model for nearly all of the rest of the structure. We further performed single-particle cryo-EM analysis of AtMRS2-1 under Mg^{2+}-free conditions in the presence of EDTA (**Figs. S4 and S5**). Interestingly, cryo-EM data processing yielded two distinct classes of EM maps at resolutions of 2.88 Å (State I)

and 3.06 Å (State II), respectively. Based on these three structures and their comparison, we discuss the Mg^{2+} permeation mechanism and conformational dynamics of AtMRS2-1.

Overall structure

First, we describe the overall architecture based on the AtMRS2-1 structure in the presence of Mg^{2+}, which was determined at the highest resolution among the three structures. AtMRS2-1 forms a symmetric funnel-like pentamer (**Figs. 1A and 1B**). Each subunit is composed of two transmembrane (TM) helices and a cytoplasmic domain consisting of long stalk helices connecting the cytoplasmic domain and TM domain, two willow helices, and six β-strands flanked by multiple short α-helices (**Figs. 1C and 1D**). The overall topology of AtMRS2-1 is largely consistent with that of other MIT family proteins (**Fig. S6**). Among them, AtMRS2-1 is structurally more similar to CtMRS2 (pentamer Cα root mean square deviation [RMSD]: 2.0 Å for 1,411 residues) than hMRS2 (Cα RMSD: 4.1 Å for 1,324 residues) and TmCorA (Cα RMSD: 3.3 Å for 1,099 residues) (**Fig. S6**). The loop region in the cytoplasmic domain (residues 144-170) that was disordered in our structure is not conserved in hMRS2 and also shows low sequence conservation among *Arabidopsis* MRS2 proteins (**Fig. S7**). Notably, the central region and the inter-subunit interfaces of the funnel-like architecture of the cytoplasmic domain are electrostatically negative (**Fig. 1E**), which may provide a favorable environment for attracting Mg^{2+}.

The ion-conducting pore of AtMRS2-1 is located at the center of the pentameric TM domain and is lined mainly by multiple hydrophilic residues of the TM1 helices (Asp367, Arg370, Glu377, Thr381, Thr384, and Asn400) (**Fig. 2A**). These residues are mostly conserved among MRS2 proteins (**Fig. S7**). Among these pore-lining residues, Asn400 is located at the luminal end of the

156 TM1 helices (**Fig. 2A**) and constitutes the conserved GMN motif in MRS2 and CorA proteins (**Fig.**
157 **S7**). As in other MIT family protein structures, the Asn400 residues form a polar ring, and an EM
158 density, presumably corresponding to a bound Mg^{2+} ion, at the site termed Site G, is observed at its
159 center (**Figs. 2B and 2C**). In CorA and other MRS2 homologs, this region has been implicated in
160 ion selectivity and is important for ion transport (24, 25, 28-32, 36-38). Consistently, the previous
161 genetic analyses of AtMRS2-1 have also suggested that this GMN motif is critical for Mg^{2+} transport
162 by AtMRS2-1 (39).

163 In the Mg^{2+}-bound structure, the pore is constricted at the Arg370 ring at the cytoplasmic end of
164 the pore (**Fig. 2A**), where the pore radius is 1.3 Å (**Fig. 5E**). This is too narrow to accommodate ion
165 conduction, indicating that Arg370 forms a barrier to ion permeation. Thus, this structure most likely
166 represents the Mg^{2+}-bound closed conformation. In addition, we observed a relatively strong density
167 at the center of the Arg370 ring. Given the positively charged nature of the side chains of the arginine
168 residues, we assigned this density to Cl^- ion (**Fig. 2D**). A similar Cl^- ion has also been reported in
169 the hMRS2 structure (28). This residue is conserved in other MRS2 proteins (**Fig. S7**), and mutation
170 of the corresponding residue affects gating properties (29, 30).

171 In the TM domain, we observed an EM density consistent with a lipid molecule at the subunit
172 interface. Interestingly, one of its acyl chains extended laterally into an inter-subunit cavity within
173 the TM domain (**Fig. S8**). This cavity is formed by Phe390 and Ala394 of TM1 and Leu416 and
174 Thr419 of TM2 from one subunit, together with Val392, Ile396, and Met399 of TM1 from the
175 adjacent subunit, thereby accommodating the hydrophobic acyl chain (**Fig. S8**). Similar lateral
176 cavities containing lipid molecules have also been observed in the structures of voltage-sensing Na^+
177 channels, mechanosensitive two-pore-domain K^+ channels, and trimeric intracellular cation (TRIC)

channels (40-44), where they have been implicated in gating modulation or structural stability. Notably, the lateral acyl chains and their surrounding residues remain largely unchanged in the Mg^{2+}-free structures (**Fig. S8**), suggesting that they may be more likely to contribute to structural stability than to gating modulation.

Cytoplasmic Mg^{2+} binding sites mediate autoinhibition

In the closed-state structure in the presence of Mg^{2+} ions, in addition to the Mg^{2+} ion and Cl^- ion bound to the TM domain, we observed multiple strong residual EM densities in the cytoplasmic domain (**Fig. 2**). Three residual EM densities were identified at each subunit interface in the distal region of the cytoplasmic domain (**Figs. 2B, 2E and 2F**). These three densities are located relatively close to one another. We assigned them as Mg^{2+} ions based on surrounding acidic residues and buffer composition (S1-S3) (**Figs. 2B, 2E and 2F**).

Among these sites, Mg^{2+} at the S1 site is coordinated by Glu331 and Glu335 from one subunit and Asp254 and Asp257 from the adjacent subunit. Mg^{2+} at the S2 site is coordinated by Asp252 and Glu331 from one subunit and Asp251 and Asp254 from the adjacent subunit. Finally, Mg^{2+} at the S3 site is coordinated by Asp250 from one subunit and Asp251 and Asp254 from the adjacent subunit. Thus, the residues involved in coordination of these Mg^{2+} ions partially overlap with one another, and the three Mg^{2+} ions together form an interaction cluster with these acidic residues at the inter-subunit interface. In addition, Mg^{2+} is known to adopt a strict hexa-coordinated geometry (2). The relatively high resolution of 2.4 Å of the Mg^{2+}-bound closed state structure allowed us to visualize EM densities likely corresponding to water molecules associated with Mg^{2+}, as well as water molecules that interact with them via amino acid residues at the cytoplasmic Mg^{2+} binding

sites (**Fig. S9**). Notably, these acidic residues are broadly conserved among *Arabidopsis* MRS2 proteins (**Fig. 3A and S7**).

Interestingly, whereas the binding site corresponding to the S1 site was also observed in the structures of hMRS2 and CtMRS2 (**Fig. 3A**), the sites corresponding to the S2 and S3 sites were not observed in either hMRS2 or CtMRS2. Consistently, the S2 and S3 sites in AtMRS2-1 involve both Asp251 and Asp254 (**Figs. 2E and 2F**), but Asp254 is not conserved in hMRS2 and Asp251 is not conserved in CtMRS2 (**Fig. 3A**). Conversely, in hMRS2 and CtMRS2, Mg^{2+} binding sites were observed at a position closer to the cytoplasmic side of the willow helices (**Figs. S6E and S6F**), whereas AtMRS2-1 lacks a Mg^{2+} binding site at the corresponding location. This is consistent with the lack of conservation in AtMRS2-1 of the residues corresponding to Glu243, Asp247, and Glu312, which form the Mg^{2+} binding site at this position in hMRS2 (**Fig. S7**). Together, these observations, combined with the conservation of the residues in the cytoplasmic Mg^{2+} binding sites identified in AtMRS2-1 among *Arabidopsis* MRS2 proteins, demonstrate that the cytoplasmic Mg^{2+} binding sites of AtMRS2-1 differ from those of MRS2 proteins from other kingdoms, including humans and fungi, thereby highlighting the diversity of cytoplasmic Mg^{2+} binding modes within the MRS2 family.

Mg^{2+} binding to the cytoplasmic domain of MRS2 and CorA channels typically stabilizes the closed state and contributes to Mg^{2+} homeostasis through autoinhibition. In the AtMRS2-1 structure, Mg^{2+} ions bound to the cytoplasmic domain also appear to fix the orientation of the cytoplasmic domain, which is connected to the TM domain via the stalk helices (**Fig. 2**), suggesting a similar role. To test this hypothesis, we performed whole-cell patch-clamp recordings of AtMRS2-1 and its cytoplasmic Mg^{2+} binding-site mutant (D251A/D254A/E257A) (**Fig. 3**). In wild-type AtMRS2-1, when $MgCl_2$ was absent from the pipette solution corresponding to the cytoplasmic side (**Fig. S1D**),

222 Mg^{2+}-dependent currents were observed upon application of Mg^{2+} in the bath solution, whereas such
223 currents were barely detectable when the pipette solution contained 1 mM $MgCl_2$ (**Fig. 3B**). These
224 results suggest that AtMRS2-1 also possesses a cytoplasmic Mg^{2+}-dependent autoinhibition
225 mechanism. Furthermore, in the cytoplasmic Mg^{2+} binding-site mutant, Mg^{2+}-dependent currents
226 were also observed when $MgCl_2$ was absent from the pipette solution corresponding to the
227 cytoplasmic side (**Fig. S1D**). However, even when the pipette solution contained 1 mM $MgCl_2$, the
228 currents were reduced but remained significant (**Fig. 3C**). These results suggest that mutations at
229 the cytoplasmic Mg^{2+}-binding sites affect cytoplasmic Mg^{2+}-dependent autoinhibition of AtMRS2-
230 1. Notably, under Mg^{2+}-free intracellular conditions, the D251A/D254A/E257A mutant showed a
231 smaller current (**Fig. 3C**), whereas its membrane surface expression level was comparable to that of
232 the wild type (**Figs. S1B and 1C).** This suggests that the D251/D254/E257 acidic cluster may
233 contribute not only to cytoplasmic Mg^{2+}-dependent autoinhibition but also to the cytoplasmic-side
234 electrostatic environment that supports efficient coupling to the conductive state. A similar
235 phenotype was also reported for human MRS2, in which alanine substitution of an intersubunit
236 acidic Mg^{2+}-binding site reduced current (30).
237
238 **Two distinct Mg^{2+}-free structures**
239 Cryo-EM analysis of AtMRS2-1 under Mg^{2+}-free conditions in the presence of EDTA yielded two
240 distinct structures (State I and State II) (**Figs. 4A-4D**). Consistent with the Mg^{2+}-free conditions, no
241 Mg^{2+} density was observed at the cytoplasmic Mg^{2+}-binding sites, and the cytoplasmic domains
242 adopted more expanded conformations, with adjacent subunits moving apart from each other (**Fig.**
243 **4E**). This is likely attributable to electrostatic repulsion in the absence of Mg^{2+}, as many of the

residues comprising the Mg^{2+}-binding sites are acidic residues (**Fig. 2**). The Mg^{2+}-bound closed-state structure is more similar to State I (Cα RMSD: 2.8 Å) than to State II (Cα RMSD: 4.3 Å). Consistently, the structural changes in the cytoplasmic Mg^{2+}-binding site were also more pronounced in State II than in State I. For example, the distance between the Cα atoms of Asp254 in one subunit and the adjacent Glu331 increased from 12.3 Å in the Mg^{2+}-bound closed state to 21.3 Å in State I and further to 28.4 Å in State II (**Fig. 4E**). The stalk helices link the cytoplasmic domain to the TM1 helices that form the ion-conduction pore (**Fig. 1**), and their distal ends participate in the formation of the Mg^{2+}-binding sites (**Fig. 2**). Thus, the different extents of conformational change in the cytoplasmic domain can lead to corresponding differences in the conformation of the TM domain.

Consistent with this notion, the larger conformational changes in the stalk helices in State II were coupled to more pronounced structural rearrangements in the TM domain (**Fig. 5A**). As a result, whereas the ion-conducting pore in State I remained essentially closed, similar to that in the Mg^{2+}-bound closed state, the pore in State II adopted a markedly expanded conformation (**Figs. 5B-5D**). Specifically, in State I, the pore remained constricted at the Arg370 ring, with a pore radius of 1.6 Å, whereas in State II, the pore radius at Arg370 was expanded to 6.0 Å (**Fig. 5E**). Thus, our State II structure may correspond to the Mg^{2+}-free open state. Consistent with this interpretation, State II closely matches the Mg^{2+}-free open-state structure of CtMRS2 (Cα RMSD: 5.0 Å for State I and 2.3 Å for State II). Moreover, our structures, all of which were reconstructed without imposing rotational symmetry (C1) (**Figs. S2-S5**), reveal symmetric conformational changes associated with channel gating in AtMRS2-1.

In contrast, although State I exhibits partial conformational changes in the cytoplasmic domain

associated with Mg^{2+} dissociation, it has not yet reached the fully open channel conformation. Thus, our State I structure may represent a previously unknown intermediate state in the structural gating cycle of the MRS2 family.

State I is important for channel opening

More detailed examination of State I revealed that near the membrane-proximal region of the cytoplasmic domain, Arg225 in the willow helix of one subunit interacted with Tyr354 and Thr358 in the stalk helix of the adjacent subunit (**Fig. 6**). Whereas this region is widely separated in State II (**Fig. 6D**), corresponding to the open state, it remains closed in State I (**Fig. 6C**), similar to the Mg^{2+}-bound closed state (**Fig. 6B**). Among these residues, Arg225 is strictly conserved in *Arabidopsis* MRS2 proteins, and Tyr354 and Thr358 are also generally conserved or replaced by residues with similar properties (**Fig. S7**). In contrast, these residues are not conserved in other representative MRS2/CorA proteins (**Fig. S7**).

To assess whether the cryo-EM-derived closed, preopen (State I), and open (State II) conformations are stable and structurally self-consistent in a membrane environment, we performed all-atom molecular dynamics (MD) simulations initiated from each state. Across three 500-ns replicates for each system, no major collapse of the starting conformations was observed (**Figs. S10A-S10C**). The Arg225-Tyr354 intersubunit separation remained short in the Mg^{2+}-bound closed and preopen systems but longer in the open system (**Figs. 6E-6G**). Consistently, the ion-conducting pore remained closed at Arg370 in the Mg^{2+}-bound closed state and State I, whereas the pore opening was maintained in State II (**Figs. S10D-S10F**).

To test the importance of these intersubunit interactions in channel gating, we performed whole-

cell patch-clamp recordings of the R225A mutant and the Y354A/T358A mutant. In parallel, we also examined the GMN motif mutant (G398A/N400A), targeting a conserved motif important for channel activity in the MRS2/CorA family, as well as the R370A mutant, targeting the pore constriction in State I (**Fig. 7**). All of these mutants showed comparable levels of cell surface expression (**Figs. S1B-1C**). Little or no current was observed for the G398A/N400A and R370A mutants, and the currents recorded from the R225A and Y354A/T358A mutants were also significantly smaller than those of the wild type (**Figs. 7B and 7C**). The loss of function in the R370A mutant suggests that Arg370 is not merely a steric barrier in the non-conducting state, but may also contribute to channel gating. These data are consistent with the possibility that Arg370 helps support the formation and/or stabilization of the State I conformation. Together, these results suggest that the interaction between Arg225 and Tyr354/Thr358 at the interface between adjacent subunits, as well as the pore architecture around Arg370, contributes to efficient channel opening. Overall, we hypothesize that State I likely represents an intermediate state in channel activation, namely a preopen state, rather than a desensitized state that follows channel activation.

Discussion

In this study, we determined the cryo-EM structure of AtMRS2-1 in the presence of Mg^{2+} (**Fig. 1**) and identified unique Mg^{2+}-binding sites in the cytoplasmic domain that are distinct from those of other MRS2 members (**Fig. 2**). We further showed that these sites are involved in cytoplasmic Mg^{2+}-dependent autoinhibition (**Fig. 3**). Similar autoinhibition has been identified not only in other MRS2 channels (28-31) but also in a distinct Mg^{2+} channel family, namely MgtE (45-47). Such a mechanism in AtMRS2-1 would provide a negative-feedback system that limits further Mg^{2+} flux

into the cytoplasm once cytoplasmic Mg^{2+} becomes sufficient. Consistently, previous studies showed that AtMRS2-1 localizes to the tonoplast (48) and participates in Mg^{2+} homeostasis by contributing to Mg^{2+} remobilization from the vacuole, particularly under Mg^{2+}-deficient conditions (20, 21). More broadly, such feedback control may help prevent excessive cytoplasmic Mg^{2+} accumulation under high-Mg conditions, for which vacuolar Mg^{2+} sequestration is protective (49, 50). In addition, residues involved in the cytoplasmic Mg^{2+}-binding sites in AtMRS2-1 are broadly conserved in rice and maize MRS2 proteins (OsMRS2 and ZmMRS2) (51, 52) (**Fig. S11**), suggesting that a similar gating mechanism may be conserved among other plant MRS2 proteins.

We also determined the structures under Mg^{2+}-free conditions and captured not only an open state (State II) but also a state in which the cytoplasmic domain is partially opened while the ion permeation pore remains closed (State I) (**Figs. 4 and 5**). Mutations of residues involved in the intersubunit interactions in this State I markedly reduced channel activity (**Figs. 6 and 7**). Together, these structural and functional analyses support the interpretation that State I represents an intermediate state along the channel-opening pathway and is consistent with a preopen state. Conceptually similar non-conducting intermediate states have been reported in other ion channels, including the preopen state captured in KcsA, the putative preopen state observed in GLIC, and the agonist-bound closed/preopen states resolved in the glycine receptor (53-55). The presence of a preopen intermediate state may allow channel activation to proceed in a stepwise manner and facilitate efficient allosteric coupling between cytoplasmic-domain rearrangement and pore opening. These observations are consistent with a stepwise gating model in which the cytoplasmic domain first adopts a partially rearranged intermediate conformation while the pore remains closed, thereby priming the TM domain for the subsequent opening transition. In addition, the residues involved in

the intersubunit interactions in the preopen state (Arg225, Tyr354, and Thr358) (**Fig. 6**) are also highly conserved in rice and maize MRS2 proteins (**Fig. S11**), suggesting that the stepwise gating mechanism through preopen-state formation may also be conserved in other plants.

Notably, all three AtMRS2-1 structures were reconstructed without imposing rotational symmetry (C1) (**Figs. S2-S5**), yet they exhibited symmetric conformational changes during gating. Together with the previously reported CtMRS2 structures (31), this observation supports the idea that symmetric gating may be conserved in eukaryotic MRS2 proteins. In this respect, eukaryotic MRS2 channels may differ from bacterial CorA, for which previous cryo-EM structural studies have been interpreted as supporting an asymmetric gating mechanism (31, 56). Consistent with this idea, the RDLR motif implicated in symmetric gating in CtMRS2 (31) is also widely conserved among *Arabidopsis* MRS2 proteins (corresponding to Arg81 to Arg84 in AtMRS2-1) (**Fig. S7**). On the basis of this framework and our results, we propose the following gating mechanism for AtMRS2-1 (**Fig. 8 and Movie S1**).

First, when cytoplasmic Mg^{2+} levels are high, Mg^{2+} binds to the cytoplasmic domain and stabilizes its arrangement, thereby maintaining the TM domain in the closed state and preventing excessive Mg^{2+} uptake (**Fig. 8A**). In contrast, when cytoplasmic Mg^{2+} levels are low, Mg^{2+} dissociates from the cytoplasmic domain. This generates electrostatic repulsion at the intersubunit Mg^{2+}-binding sites, which are enriched in acidic residues, and promotes conformational changes that separate adjacent subunits (**Fig. 8B**). As an initial step toward channel opening, the cytoplasmic domain may adopt a partially rearranged intermediate state (State I), in which the pore remains closed and which is consistent with a preopen conformation (**Fig. 8B**). In this state, the interaction between Arg225 and Tyr354/Thr358 appears to stabilize the non-conducting intermediate state (**Fig. 8B**). Because the

cytoplasmic rearrangement involves the stalk helices, which connect the cytoplasmic domain to the pore-forming TM1 helices, these conformational changes can be transmitted to the TM domain. These conformational changes may then lead to opening of the Arg370 constriction site and formation of the fully open state (State II), thereby allowing Mg2+ permeation (**Fig. 8C**). Taken together, this study elucidates the structural basis for a unique gating mechanism and its regulation in plant MRS2, including a distinct cytoplasmic Mg^{2+}-binding site and stepwise gating involving a preopen state, both of which differ from those of other MRS2 channels such as the human homolog.

Methods

Protein expression and purification

The coding region (residues 44-442) of *Arabidopsis thaliana* MRS2-1 (AtMRS2-1, UniProt ID: Q9S9N4) was synthesized (Genewiz, China) and subcloned into the pFastBac vector with a C-terminal human rhinovirus 3C (HRV 3C) protease cleavage site, monomeric ultra-stable GFP (muGFP) (57), and Twin-Strep-tag. DH10Bac *Escherichia coli* cells (Gibco, USA) were used as the host for bacmid recombination. Sf9 cells were cultured in suspension at 27 °C in SIM SF culture medium (Sino Biological, China) and routinely passaged every other day. The initial recombinant baculovirus was generated by transfecting adherent Sf9 cells with bacmid DNA using FuGENE HD reagent (Promega, USA), and was subsequently used to infect suspension cells for virus amplification. The protein was overexpressed in suspension-cultured Sf9 cells at 27 °C for 72 h after virus infection. Cells were collected and lysed by sonication in TBS buffer (50 mM Tris-HCl, pH 8.0, 150 mM NaCl) with 2 mM β-Mercaptoethanol (β-ME), 1 mM phenylmethylsulfonyl fluoride (PMSF), 5.2 μg/mL aprotinin, 2 μg/mL leupeptin and 1.4 μg/mL pepstatin A. The supernatant was

collected after centrifugation at 7,500 × g for 20 min and then ultracentrifuged at 200,000 × g for 1 h. The membrane fraction pellets were collected and solubilized in solubilization buffer [50 mM Tris-HCl, pH 8.0, 150 mM NaCl, 1% Lauryl Maltose Neopentyl Glycol (LMNG) (Anatrace, USA)] with 2 mM β-ME, 1 mM PMSF, 5.2 μg/mL aprotinin, 2 μg/mL leupeptin, 1.4 μg/mL pepstatin A and the suspension was stirred for 2 h. The solubilized mixture was ultracentrifuged at 200,000 × g for 1 h. The supernatant was loaded onto Strep-Tactin Superflow Plus beads (Qiagen, USA) pre-equilibrated with the wash buffer [50 mM Tris-HCl, pH 8.0, 150 mM NaCl, 2 mM β-ME and 0.02% Glycol-Diosgenin (GDN) (Anatrace, USA)] and stirred for 2 h. The resin was washed with 10 CV of the wash buffer. The proteins were eluted by elution buffer (50 mM Tris-HCl, pH 8.0, 150 mM NaCl, 0.02% GDN, 2 mM β-ME, 2.5 mM desthiobiotin). HRV3C was used to remove C-terminal muGFP and Twin-Strep-tag at a ratio of 1:5 (w:w) overnight, and the sample was then subjected to size-exclusion chromatography (SEC) on a Superdex 200 Increase 10/300 GL column (Cytiva, USA) pre-equilibrated with SEC buffer [150 mM NaCl, 20 mM HEPES, pH 7.5, 0.5 mM Tris (2-carboxyethyl) phosphine (TCEP), 0.01% GDN]. Peak fractions were collected and concentrated to 15 mg/mL using an Amicon Ultra 100 kDa cutoff. All purification steps were performed at 4 °C.

Cryo-EM data acquisition

For grid preparation, purified AtMRS2-1 was incubated with either 5 mM $MgCl_2$ or 5 mM EDTA for 1 h. 2.5 μL of the AtMRS2-1 sample was applied to holey carbon-film grids (Quantifoil, Germany, Au R1.2/1.3 μm size/hole space, 300 mesh) glow-discharged for 60 s, blotted with a Vitrobot (Thermo Fisher Scientific, USA) with 95% humidity at 4 °C and plunge-frozen in liquid ethane cooled by liquid nitrogen.

For the dataset of AtMRS2-1 with 5 mM $MgCl_2$, cryo-EM datasets were acquired with a Krios G4 (Thermo Fisher Scientific, USA) electron microscope equipped with a Falcon 4i direct electron detector (Thermo Fisher Scientific, USA). A total of 3,102 movie stacks of 40 frames were collected at an acceleration voltage of 300 kV with a magnification of 130,000×, a pixel size of 0.959 Å/pix, and defocus range from −1.0 μm to −1.5 μm. The dose rate was 8 e-/s, and the exposure time was 4.60 s, with an exposure of 40 e-/$Å^2$.

For the dataset of AtMRS2-1 with 5 mM EDTA, cryo-EM datasets were acquired with a Titan Krios (Thermo Fisher Scientific, USA) electron microscope equipped with a K3 direct electron detector (Gatan Inc., USA). A total of 8,216 movie stacks of 40 frames were collected at an acceleration voltage of 300 kV with a magnification of 81,000×, a pixel size of 0.894 Å/pix, and defocus range from −1.0 μm to −2.2 μm. The dose rate was 16 e-/s, and the exposure time was 2.12 s, with an exposure of 50 e-/$Å^2$.

Cryo-EM data processing

The overall workflow of image processing is illustrated in **Figs. S2-S5**. All processing was performed within cryoSPARC v4.412 (58-60). Movies were processed using patch motion correction and patch CTF estimation.

For the dataset of AtMRS2-1 with 5 mM $MgCl_2$, particles were extracted from template picking at 1× binned with a box size of 256 px (~246 Å) and then subjected to 2D classification to remove junk particles. Particles were then subjected to ab-initio reconstruction and 2 rounds of heterogeneous refinement with C1 symmetry (K=6) to further sort particles. These selected particles were then re-extracted at 1× binned with a box size of 320 px (~307 Å), followed by non-uniform

refinement (C5), local CTF refinement, and symmetry expansion according to C5 symmetry. The full mask output at the non-uniform refinement step was used as the initial mask for the subsequent local refinement step. The local refinement procedure produced a final map with a resolution of 2.44 Å (Closed state), (using the Fourier shell correlation = 0.143 cutoff criterion) with C1 symmetry (**Table S1**).

For the dataset of AtMRS2-1 with 5 mM EDTA, particles were extracted from template picking at 4× binned with a box size of 320 px (~286 Å) and then subjected to 2D classification to remove junk particles. Particles were then subjected to ab-initio reconstruction and 3 rounds of heterogeneous refinement with C1 symmetry (K=6). Two classes were selected and then performed with another heterogeneous refinement with C5 symmetry (K=2) to further sort particles. Particles of these two classes were re-extracted respectively at 1× binned with a box size of 320 px (~286 Å), followed by non-uniform refinement (C5), local CTF refinement, and symmetry expansion according to C5 symmetry. For both classes, the full mask output at the non-uniform refinement step was used as the initial mask for the subsequent local refinement step. The local refinement procedure produced a final map with a resolution of 2.88 Å (State I: Preopen state) and 3.06 Å (State II: Open state), respectively (using the Fourier shell correlation = 0.143 cutoff criterion) with C1 symmetry (**Table S1**).

Model building and refinement

Model building was initiated using a predicted AtMRS2-1 model generated using the ColabFold version of AlphaFold2 (61, 62). Docking of the template model into the cryo-EM maps was performed in PHENIX (63). The models were manually adjusted in Coot (64), followed by real-

space refinement in PHENIX (**Table S1**). In the final models, each subunit included residues 49-143 and 171-441 for the Mg^{2+}-bound closed state, residues 49-143 and 177-437 for State I (preopen), and residues 48-143 and 174-437 for State II (open). Structure figures were generated using UCSF Chimera 1.175 (65) and PyMOL (https://pymol.org/). The sequence alignment figure was generated using Clustal Omega (66) and ESPript 3.2 (67). The ion permeation pathway was calculated using HOLE (68).

Electrophysiology

The AtMRS2-1 ΔN43 construct and its mutants for mammalian cell expression were synthesized by Genewiz (China), codon-optimized for human expression, and subcloned into the pCDNA5 vector containing an N-terminal putative polycysteine palmitoylation motif (YQFECCCCESLVGGGCC) to facilitate cell surface expression and a C-terminal GFP tag.

Human embryonic kidney (HEK293T) cells used were cultured in DMEM medium supplemented with 1% penicillin/streptomycin (Gibco, USA), 1% glutamate (Gibco, USA) and 10% FBS (PAN-Biotech, Germany) at 37°C in a humidified atmosphere of 5% CO2 and 95% air. Plasmids encoding the AtMRS2-1 ΔN43 construct and its mutants were transiently transfected into HEK293T cells using the calcium phosphate method (69).

Electrophysiological recordings were conducted on HEK293T cells after transfection for 24-48 h at 23 ± 2 °C. In the whole-cell configuration under voltage clamp, patch pipettes filled with pipette solution were used, with resistance ranging from 3 to 5 MΩ. Pipette solutions of two distinct compositions were applied for whole-cell current recordings of the AtMRS2-1 ΔN43 construct and its mutants: The standard Mg^{2+}-free intracellular pipette solution contained (in mM) 120 Cs-

glutamate, 8 NaCl, 10 Cs-EGTA, 5 Cs-EDTA, 10 HEPES–CsOH, pH 7.2 (70), or the 1 mM Mg^{2+} intracellular pipette solution contained (in mM) 116 Cs-glutamate, 8 NaCl, 10 Cs-EGTA, 10 HEPES-CsOH, 1 $MgCl_2$, pH 7.2. The standard external solution used to perfuse during electrophysiological recordings contained (in mM) 150 NaCl, 5 KCl, 10 EGTA, 10 glucose, and 10 HEPES with pH adjusted to 7.4 using Tris-base. $MgCl_2$ (20 or 40 mM) was added to the standard external solution for stimulating the AtMRS2-1 ΔN43 construct and its mutants. During electrophysiological recordings, a Y-tube was used to continuously perfuse solutions throughout the experiments. The EZ Patch integrated patch-clamp system (Elements Instruments, Italy) was used for all current signal amplification and data acquisition; current data were sampled at 10 kHz, with low-pass filtering at 0.25 kHz. Data analysis was performed using Clampex and Clampfit 10.6 software (Molecular Devices, USA). Throughout the experiment, the membrane potential was maintained at −60 mV under voltage-clamp conditions (71).

Western blotting

HEK293T cells transfected with the AtMRS2-1 ΔN43 construct or its mutants were washed with cold phosphate-buffered saline (PBS) solution (pH 7.0) and then incubated with sulfo-NHS-LC-biotin (Pierce) dissolved in cold $PBS^{+/+}$(containing 1 mM $MgCl_2$ and 0.1 mM $CaCl_2$, pH 8.0) at low temperature for 30 min. Glycine (20 mM) was then added to cells and incubated for 20 min to halt the reaction. The cells were collected and lysed with Radio-Immunoprecipitation Assay (Thermo Scientific, USA) lysis buffers after washing 3 times with cold PBS solution (pH 7.4). After high-speed centrifugation, the lysate was incubated with NeutrAvidin agarose resin (Thermo Scientific, USA) overnight at 4 °C. Subsequently the resin was washed 3-5 times with chilled PBS and diluted

with SDS loading buffer and used as the surface protein fraction. The protein samples were separated by SDS-polyacrylamide gel electrophoresis (PAGE) (NCM Biotech, China) and transferred to a polyvinylidene difluoride (PVDF) membrane (Immobilon-P). The PVDF membrane was blocked with 5% milk (Difco, USA) at room temperature for 1 to 2 h and then incubated overnight at 4 °C with anti-GFP (1:2000)(Sigma, USA), anti-Na^+/K^+-ATPase (1:2000)(ABclonal, China) or anti-GAPDH (1:3000) (Sungene Biotech, China) antibodies dissolved in 5% milk. The PVDF membrane was washed 4 to 5 times with Tris Buffered Saline with Tween 20. The membrane was then incubated with appropriate horseradish peroxidase (HRP)-conjugated secondary antibodies: goat anti-mouse IgG (H+L)-HRP for anti-GFP, and goat anti-rabbit IgG (H+L)-HRP for anti-GAPDH or anti-Na^+/K^+-ATPase (25 °C, 1 h, 1:2000). Finally, protein expression was visualized by exposure with automated chemiluminescence-fluorescence image analysis systems (Tanon 5200 Multi) (Tanon, China) for 1 to 3 min in ECL solution (Thermo Scientific, USA). Analysis of protein expression was repeated by at least three independent experiments (72, 73).

Molecular dynamics simulations

The initial coordinates of the Mg^{2+}-bound closed state, State I (preopen), and State II (open) conformations of AtMRS2-1 were taken from the corresponding cryo-EM structures (**Table S2**). Missing residues were modeled using Modeller (74, 75). Protonation states of titratable residues at pH 7.0 were assigned using PropKa (76). Mg^{2+} ions, Cl^- ions, and associated water molecules observed in the cryo-EM structures were retained. Experimentally resolved lipid molecules were also preserved where present. The composition of ions and POPC lipids was further adjusted for each simulation system according to the specific state being modeled. The prepared protein

structures were embedded into a POPC lipid bilayer using CHARMM-GUI (77), with the initial membrane-insertion position derived from the Orientations of Proteins in Membranes (OPM) database (78). The systems were then solvated with explicit TIP3P (79) water molecules, and KCl was added to a final concentration of 150 mM to mimic physiological ionic strength while maintaining overall charge neutrality.

All simulations were performed using GROMACS 2018.3 (80) with the CHARMM36 (81) force field for proteins and lipids. Energy minimization was first performed using the steepest descent algorithm until convergence. During this step, positional restraints (10000 $kJ \cdot mol^{-1} \cdot nm^{-2}$) were applied to the protein heavy atoms, lipid headgroups, and ions to stabilize the initial configuration. The temperature was maintained at 303 K using the Nosé–Hoover (82, 83) thermostat, and pressure was maintained at 1 bar using the Parrinello–Rahman (84) barostat with semi-isotropic pressure coupling.

All covalent bonds involving hydrogen atoms were constrained using the LINCS (85) algorithm, allowing a 2 fs integration time step. Long-range electrostatic interactions were computed via the particle mesh Ewald (PME) (86) method, and the cutoff distance for both electrostatic and van der Waals interaction was set to 1.2 nm. During equilibration, positional restraints on lipid molecules were gradually released to allow full relaxation of the membrane bilayer, while restraints on the protein backbone were progressively reduced.

After equilibration, 500-ns production simulations were carried out for each system without restraints. Three independent trajectories were generated for each system using different initial velocity seeds.

Data availability

The atomic coordinates of AtMRS2-1 were deposited in the Protein Data Bank under accession codes 24PF (Mg^{2+}-bound closed) [http://doi.org/10.2210/pdb24PF/pdb], 24PG (State I, Mg^{2+}-free preopen) [http://doi.org/10.2210/pdb24PG/pdb], and 24PH (State II, Mg^{2+}-free open) [http://doi.org/10.2210/pdb24PH/pdb], respectively. Cryo-EM maps were deposited in the Electron Microscopy Data Bank (EMDB) under accession codes EMD-69740 (Mg^{2+}-bound closed) [https://www.ebi.ac.uk/pdbe/entry/emdb/EMD-69740], and EMD-69741 (State I, Mg^{2+}-free preopen) [https://www.ebi.ac.uk/pdbe/entry/emdb/EMD-69741] and EMD-69742 (State II, Mg^{2+}-free open) [https://www.ebi.ac.uk/pdbe/entry/emdb/EMD-69742], respectively. The raw current trace data and uncropped raw western blot images are deposited in Mendeley Data (https://doi.org/10.17632/2rwg5nr9ht). All other relevant data are included in the paper or its supporting information.

Acknowledgments

We thank the staff scientists at the Cryo-EM Facility of the School of Life Sciences, Fudan University and the National Center for Protein Science Shanghai (Chinese Academy of Sciences, project numbers: 2024-NFPS-PT-008125 and 2024-NFPS-PT-008367) for technical assistance with cryo-EM data collection. This work was supported by funding from the National Natural Science Foundation of China to M.H. (32471247, 32271244, 32411540020, and 32071234). This work was also supported by the Open Research Fund of State Key Laboratory of Genetics and Development of Complex Phenotypes (No. SKLGDP2502, M. H.).

552

Figure Legends

Figure 1. Overall structure of AtMRS2-1.

(A) The cryo-EM density map of the AtMRS2-1 homopentamer in the Mg^{2+}-bound closed state, viewed from the membrane plane (upper), from the lumen (lower left) and from the cytoplasm (lower right). Each protomer is colored red, yellow, green, blue and purple, respectively, and the lipid molecules are colored gray. (B) The structure of AtMRS2-1 in the Mg^{2+}-bound closed state, with the same views and coloring scheme. (C) Cartoon representation of the AtMRS2-1 protomer. (D) Schematic diagram outlining the topology of the AtMRS2-1 protomer, colored as in panel (C). (E) The electrostatic surface potential of the AtMRS2-1 homopentamer, shown from the membrane plane (left), from the lumen (upper right) and from the cytoplasm (lower right).

Figure 2. The pore architecture and cytoplasmic Mg^{2+} binding sites in the closed state.

(A) The central ion pathway, estimated using HOLE and represented as a surface. Two opposite subunits are shown for clarity, with residues lining the pathway shown as sticks. (B) The model of two adjacent subunits showing the ion binding sites of AtMRS2-1 in the closed state. Ions are shown as spheres of different colors. (C-F) The ion-binding sites, including Mg^{2+}-Site G (C), Cl^{-}-Site (D), and Mg^{2+}-Site S1, S2 and S3 (E-F). Mg^{2+} ions are colored green, and the Cl^{-} ion is colored orange. The EM density maps for the ions are shown in black mesh and contoured at 4.0 σ (C), 4.0 σ (D), 6.0 σ (E), and 6.0 σ (F), respectively. The residues around these ions are shown as sticks.

Figure 3. Cytoplasmic Mg^{2+}-binding site-dependent autoinhibition.

(A) Sequence alignment of MRS2 proteins: MRS2 from *Arabidopsis thaliana* (AtMRS2-1: Q9S9N4,

AtMRS2-2: Q9FLG2, AtMRS2-3: Q9LJN2, AtMRS2-4: Q93ZD7, AtMRS2-5: Q9ZPR4, AtMRS2-6: Q1PE39, AtMRS2-7: Q304A0, AtMRS2-10: Q9SAH0, AtMRS2-11: Q058N4), MRS2 *from Homo sapiens* (Q9HD23), *Chaetomium thermophilum* (G0S186), and CorA from *Thermotoga maritima* (Q9WZ3). Only the residues around the cytoplasmic Mg^{2+} binding sites are shown. Green circles indicate Mg^{2+} binding sites. The sequence numbering of AtMRS2-1 is shown. (B) Whole-cell patch-clamp traces from HEK293T cells expressing AtMRS2-1 ΔN43 construct and D251A/D254A/E257A mutant exposed to 20 and 40 mM Mg^{2+} with intracellular pipette solution containing 1 mM Mg^{2+}. (C) Pooled data of AtMRS2-1 ΔN43 construct and its mutant induced by 20 mM Mg^{2+}. Bars represent mean ± S.E. from n = 6, * $P < 0.05$; ** $P < 0.01$ vs. WT, unpaired t-test.

Figure 4. Overall structures of AtMRS2-1 in the presence of EDTA.

(A, B) The cryo-EM density map (A) and the structural model (B) of the AtMRS2-1 homopentamer in the presence of EDTA (State I), shown from the membrane plane. (C, D) The cryo-EM density map (C) and the structural model (D) of the AtMRS2-1 homopentamer in the presence of EDTA (State II), shown from the membrane plane. (E) Superimposition of the three state structures of AtMRS2-1 (Closed state: red; State I: green; State II: blue). Only two adjacent subunits are shown. Mg^{2+} ions in the cytoplasmic domain of the closed state structure are shown as spheres and colored green. Dotted lines indicate the distance (Å) between the Cα atoms of Asp254 and Glu331 in two adjacent subunits.

Figure 5. Structural comparison of the pore architectures of AtMRS2-1.

(A) Superimposition of the three state structures (Closed state: red; State I: green; State II: blue). Only TM1, TM2, and the stalk helices from two adjacent subunits are shown. (B, C) The central ion pathway for State I (B) and State II (C), estimated using HOLE and represented as a surface. Two opposite subunits are shown for clarity, with residues lining the pathway shown as sticks. (D) Structural comparison of the three states at the pore constriction formed by Arg370 (Closed state: red; State I: green; State II: blue). (E) Pore radius profiles along the central axis for the three states.

Figure 6. State-specific intersubunit interactions.

(A) Superimposition of the three states of AtMRS2-1 (Closed state: red; State I: green; State II: blue). Only two adjacent subunits are shown. (B-D) Close-up views of the upper region of the stalk helix and willow helices in the closed state (B), State I (C), and State II (D). The side chains of Arg225 (from one subunit) and Tyr354 and Thr358 (from the adjacent subunit) are shown in stick representation. Dotted lines indicate hydrogen bonding. (E-G) MD simulations of AtMRS2-1 structures in the closed state (E), State I (F) and State II (G). Distance plots between the Cα atoms of Arg225 and Tyr354 between the two adjacent subunits are shown.

Figure 7. Mutational analysis of pore-lining and intersubunit interaction residues.

(A) Sequence alignment of MRS2 proteins. Only the residues around the intersubunit interactions are shown. Purple triangles represent the residues involved in intersubunit interactions. The sequence numbering of AtMRS2-1 is shown. (B) Whole-cell patch-clamp traces from HEK293T cells expressing AtMRS2-1 ΔN43 construct and its mutants exposed to 20 mM Mg^{2+} with Mg^{2+}-free intracellular pipette solution. (C) Pooled data of AtMRS2-1 ΔN43 construct and its mutants

619 induced by 20 mM Mg^{2+}. Bars represent mean ± S.E. from n = 4-10, * P < 0.05; ** P < 0.01 vs.
620 WT, one-way ANOVA followed by Dunnett's multiple-comparisons test. F(2,17) = 10.45.
621
622 **Figure 8. Putative gating mechanism of AtMRS2-1.**
623 (**A-C**) Cartoon diagrams depicting the conformational changes associated with cytoplasmic Mg^{2+}-
624 dependent gating of AtMRS2-1. The panels show the closed (A), preopen (State I) (B), and open
625 (State II) (C) states. Mg^{2+} ions are shown as green spheres, and key residues are depicted as sticks.
626
627 **Supplementary Figure Legends**
628 **Figure S1. Purification and electrophysiology of AtMRS2-1.**
629 (A) Size-exclusion chromatography of GFP-fused AtMRS2-1 ΔN43, as detected by UV absorbance.
630 (B) Representative western blot analysis of cell-surface expression of AtMRS2-1 ΔN43 and its
631 mutants in transfected HEK293T cells. Cell-surface proteins were labeled by sulfo-NHS-LC-biotin
632 and isolated with NeutrAvidin agarose resin. Na^+/K^+-ATPase was used as a plasma membrane
633 marker. The blot shown is representative of three independent experiments. (C) Quantification of
634 the cell-surface expression shown in (B), normalized to AtMRS2-1 ΔN43. Bars represent mean ±
635 S.E., P > 0.05, one-way ANOVA followed by Dunnett's multiple comparisons test, F (5, 10) = 1.94.
636 (D) Whole-cell patch-clamp traces from HEK293T cells expressing ΔN43 construct and the
637 D251A/D254A/E257A mutant exposed to 20 and 40 mM Mg^{2+} with Mg^{2+}-free intracellular pipette
638 solution.
639
640 **Figure S2. Cryo-EM data processing workflow for AtMRS2-1 with 5 mM $MgCl_2$.**

All processing steps were performed in CryoSPARC. Images were generated using UCSF Chimera.

Figure S3. Cryo-EM analysis of AtMRS2-1 with 5 mM $MgCl_2$.

(A) Representative cryo-EM micrograph of AtMRS2-1 with 5 mM $MgCl_2$. (B) Representative 2D class averages. (C) The gold-standard Fourier shell correlation (FSC) curves for resolution estimation. (D) Angular distribution of the particles used for the final map. (E-G) Top view from the lumen side (E), bottom view from the cytoplasmic side (F), and side view (G) of the EM density map, colored according to the local resolution, estimated using CryoSPARC.

Figure S4. Cryo-EM data processing workflow for AtMRS2-1 with 5 mM EDTA.

All processing steps were performed in CryoSPARC. Images were generated using UCSF Chimera.

Figure S5. Cryo-EM analysis of AtMRS2-1 with 5 mM EDTA.

(A) Representative cryo-EM micrograph of AtMRS2-1 with 5 mM EDTA. (B) Representative 2D class averages. (C, D) The gold-standard Fourier shell correlation (FSC) curves for resolution estimation of State I (C) and State II (D). (E, F) Angular distribution of the particles used for the final map of State I (E) and State II (F). (G-I) Top view from the lumen side (G), bottom view from the cytoplasmic side (H), and side view (I) of the State I EM density map, colored according to the local resolution, estimated using CryoSPARC. (J-L) Top view from the lumen side (J), bottom view from the cytoplasmic side (K), side view (L) of the State II EM density map, colored according to the local resolution, estimated using CryoSPARC.

Figure S6. Structural comparison with MRS2/CorA proteins.

(A-C) Alignments of AtMRS2-1 in the closed state (wheat) with CtMRS2 in the closed state (light blue, PDB ID: 8Q8P) (A), hMRS2 in the closed state (pink, PDB ID: 8IP3) (B), and TmCorA in the closed state (green, PDB ID: 3JCF) (C). The left panel shows an alignment of the pentamers, while the right panel displays an alignment of the monomers. (D) Alignments of AtMRS2-1 in State II (orange) with CtMRS2 in the open state (purple, PDB ID: 8Q8Q). The left panel shows an alignment of the pentamers, while the right panel displays an alignment of the monomers. (E-G) Close-up views of the corresponding Mg^{2+}-binding sites in CtMRS2 (PDB ID: 8Q8P) (E), hMRS2 (PDB ID: 8IP3) (F) and TmCorA (green, PDB ID: 3JCF) (G).

Figure S7. Sequence alignment.

AtMRS2-1 (UniProt ID: Q9S9N4), AtMRS2-2 (UniProt ID: Q9FLG2), AtMRS2-3 (UniProt ID: Q9LJN2), AtMRS2-4 (UniProt ID: Q93ZD7), AtMRS2-5 (UniProt ID: Q9ZPR4), AtMRS2-6 (UniProt ID: Q1PE39), AtMRS2-7 (UniProt ID: Q304A0), AtMRS2-10 (UniProt ID: Q9SAH0), AtMRS2-11 (UniProt ID: Q058N4), hMRS2 (UniProt ID: Q9HD23), CtMRS2 (UniProt ID: G0S186), and TmCorA (UniProt ID: Q9WZ3) were aligned. The sequence number of AtMRS2-1 is shown. Green and orange circles indicate Mg^{2+} binding sites, and Arg370, respectively. The blue rectangle and purple triangle represent the GMN motif and the amino acids related to intersubunit interactions, respectively.

Figure S8. Lateral lipid binding in AtMRS2-1.

(A-I) Lateral lipid binding sites of AtMRS2-1 in the closed state (A-C), State I (D-F), and State II

(G-I). Densities for lipids are shown in gray mesh, contoured at 4.0 σ. Side chains of interaction-related amino acids are shown in stick representation.

Figure S9. The EM density maps for the cytoplasmic Mg^{2+} ions and water molecules.

(A-C) The EM density maps for Mg^{2+} ions and water molecules at the cytoplasmic Mg^{2+} binding sites are shown in gray mesh and contoured at 3.0σ (A), 3.5σ (B), and 4.0σ (C), respectively. The residues around these ions and water molecules are shown as sticks. (D) Schematic diagram of the interaction network involving Mg^{2+} ions at sites S1-S3, water molecules, and residues of AtMRS2-1. Mg^{2+} ions and water molecules are shown as green and red spheres, respectively. Key residues from one subunit are shown as blue spheres, whereas those from the adjacent subunit are shown as green spheres. Dotted lines indicate interactions.

Figure S10. MD simulations.

(A-C) The plots of the RMSD of the Cα atoms are shown for the closed state (A), State I (B), and State II (C) structures. (D–F) Distance plots showing the distance between the Arg370 Cα atoms and the center point (defined as the average position of the five subunits) are shown for the closed state (D), State I (E), and State II (F) structures.

Figure S11. Sequence alignment with other plant MRS2 proteins.

Sequence alignment among AtMRS2-1 (UniProt ID: Q9S9N4), AtMRS2-2 (UniProt ID: Q9FLG2), AtMRS2-3 (UniProt ID: Q9LJN2), AtMRS2-4 (UniProt ID: Q93ZD7), AtMRS2-5 (UniProt ID: Q9ZPR4), AtMRS2-6 (UniProt ID: Q1PE39), AtMRS2-7 (UniProt ID: Q304A0), AtMRS2-10

(UniProt ID: Q9SAH0), AtMRS2-11 (UniProt ID: Q058N4), OsMRS2-A (UniProt ID: Q9AUK4), OsMRS2-B (UniProt ID: Q67UQ7), OsMRS2-C (UniProt ID: Q0JBZ6), OsMRS2-D (UniProt ID: Q7XQQ1), OsMRS2-E (UniProt ID: Q8S1N1), OsMRS2-F (UniProt ID: Q8L4S2), OsMRS2-G (UniProt ID: A3BV82), OsMRS2-H (UniProt ID: Q10S25), OsMRS2-I (UniProt ID: Q10D38), ZmMRS2-A (UniProt ID: A0A317Y4T9), ZmMRS2-B_1 (UniProt ID: A0A3L6DDP3), ZmMRS2-D (UniProt ID: A0A3L6G7L2), ZmMRS2-E (UniProt ID: A0A3L6FS80), ZmMRS2-F_0 (UniProt ID: A0A3L6DNR6), ZmMRS2-G_0 (UniProt ID: A0A8J8XSX0), ZmMRS2-G_1 (UniProt ID: A0A8J8XLQ5), ZmMRS2-H (UniProt ID: A0A317YB95), ZmMRS2-I (UniProt ID: A0A317Y479), hMRS2 (UniProt ID: Q9HD23), CtMRS2 (UniProt ID: G0S186), TmCorA (UniProt ID: Q9WZ3). The sequence numbering of AtMRS2-1 is shown. Green circles and purple triangles indicate Mg^{2+} binding sites and amino acids involved in intersubunit interactions, respectively.

Table S1. Cryo-EM data collection, refinement and validation statistics.

Table S2. Summary of molecular dynamics simulation systems and trajectories.

Movie S1. Conformational changes of AtMRS2-1.

Data S1. Numerical raw data.

References

1. J. H. de Baaij, J. G. Hoenderop, R. J. Bindels, Magnesium in man: implications for health and disease. *Physiol Rev* **95**, 1-46 (2015).
2. M. E. Maguire, J. A. Cowan, Magnesium chemistry and biochemistry. *Biometals : an international journal on the role of metal ions in biology, biochemistry, and medicine* **15**, 203-210 (2002).
3. A. Hartwig, Role of magnesium in genomic stability. *Mutation research* **475**, 113-121 (2001).
4. J. A. Cowan, Structural and catalytic chemistry of magnesium-dependent enzymes. *Biometals : an international journal on the role of metal ions in biology, biochemistry, and medicine* **15**, 225-235 (2002).
5. N. Verbruggen, C. Hermans, Physiological and molecular responses to magnesium nutritional imbalance in plants. *Plant and Soil* **368**, 87-99 (2013).
6. J. Gerendás, H. Führs, The significance of magnesium for crop quality. *Plant and Soil* **368**, 101-128 (2013).
7. I. Cakmak, E. A. Kirkby, Role of magnesium in carbon partitioning and alleviating photooxidative damage. *Physiol Plant* **133**, 692-704 (2008).
8. W. Guo, H. Nazim, Z. Liang, D. Yang, Magnesium deficiency in plants: An urgent problem. *The Crop Journal* **4**, 83-91 (2016).
9. V. Knoop, M. Groth-Malonek, M. Gebert, K. Eifler, K. Weyand, Transport of magnesium and other divalent cations: evolution of the 2-TM-GxN proteins in the MIT superfamily. *Mol Genet Genomics* **274**, 205-216 (2005).
10. D. Niegowski, S. Eshaghi, The CorA family: structure and function revisited. *Cellular and molecular life sciences : CMLS* **64**, 2564-2574 (2007).
11. K. M. Papp-Wallace *et al.*, The CorA Mg^{2+} channel is required for the virulence of Salmonella enterica serovar typhimurium. *J Bacteriol* **190**, 6517-6523 (2008).
12. Y. Park *et al.*, Inhibition of CorA-Dependent Magnesium Homeostasis Is Cidal in Mycobacterium tuberculosis. *Antimicrob Agents Chemother* **63** (2019).
13. D. Chatterjee *et al.*, Involvement of CorA of Mycobacterium smegmatis in exerting intrinsic resistance towards structurally unrelated antibiotics. *J Appl Microbiol* **135** (2024).
14. M. Piskacek, L. Zotova, G. Zsurka, R. J. Schweyen, Conditional knockdown of hMRS2 results in loss of mitochondrial Mg^{2+} uptake and cell death. *J Cell Mol Med* **13**, 693-700 (2009).
15. Y. Chen *et al.*, Human mitochondrial Mrs2 protein promotes multidrug resistance in gastric cancer cells by regulating p27, cyclin D1 expression and cytochrome C release. *Cancer Biol Ther* **8**, 607-614 (2009).
16. T. Kuramoto *et al.*, A mutation in the gene encoding mitochondrial Mg^{2+} channel MRS2 results in demyelination in the rat. *PLoS genetics* **7**, e1001262 (2011).
17. I. Schock *et al.*, A member of a novel Arabidopsis thaliana gene family of candidate Mg^{2+} ion transporters complements a yeast mitochondrial group II intron-splicing mutant. *Plant J* **24**, 489-501 (2000).
18. L. Li, A. F. Tutone, R. S. Drummond, R. C. Gardner, S. Luan, A novel family of magnesium transport genes in Arabidopsis. *Plant Cell* **13**, 2761-2775 (2001).
19. B. M. Waters, Moving magnesium in plant cells. *New Phytol* **190**, 510-513 (2011).
20. H. Lenz *et al.*, Magnesium deficiency phenotypes upon multiple knockout of Arabidopsis thaliana MRS2 clade B genes can be ameliorated by concomitantly reduced calcium supply. *Plant Cell Physiol* **54**, 1118-1131 (2013).

21. R. J. Tang *et al.*, Two transporters mobilize magnesium from vacuolar stores to enable plant acclimation to magnesium deficiency. *Plant Physiol* **190**, 1307-1320 (2022).
22. M. Gebert *et al.*, A root-expressed magnesium transporter of the MRS2/MGT gene family in Arabidopsis thaliana allows for growth in low-Mg^{2+} environments. *Plant Cell* **21**, 4018-4030 (2009).
23. Y. Sun, R. Yang, L. Li, J. Huang, The Magnesium Transporter MGT10 Is Essential for Chloroplast Development and Photosynthesis in Arabidopsis thaliana. *Mol Plant* **10**, 1584-1587 (2017).
24. V. V. Lunin *et al.*, Crystal structure of the CorA Mg^{2+} transporter. *Nature* **440**, 833-837 (2006).
25. S. Eshaghi *et al.*, Crystal structure of a divalent metal ion transporter CorA at 2.9 angstrom resolution. *Science* **313**, 354-357 (2006).
26. J. Payandeh, E. F. Pai, A structural basis for Mg^{2+} homeostasis and the CorA translocation cycle. *The EMBO journal* **25**, 3762-3773 (2006).
27. F. Jin, Y. Huang, M. Hattori, Recent advances in the structural biology of Mg^{2+} channels and transporters. *Journal of Molecular Biology* **434**, 167729 (2022).
28. M. Li *et al.*, Molecular basis of Mg^{2+} permeation through the human mitochondrial Mrs2 channel. *Nat Commun* **14**, 4713 (2023).
29. L. T. F. Lai, J. Balaraman, F. Zhou, D. Matthies, Cryo-EM structures of human magnesium channel MRS2 reveal gating and regulatory mechanisms. *Nat Commun* **14**, 7207 (2023).
30. Z. He *et al.*, Structure and function of the human mitochondrial MRS2 channel. *Nat Struct Mol Biol* **32**, 459-468 (2025).
31. P. Li *et al.*, Closed and open structures of the eukaryotic magnesium channel Mrs2 reveal the auto-ligand-gating regulation mechanism. *Nat Struct Mol Biol* **32**, 491-501 (2025).
32. O. Dalmas *et al.*, A repulsion mechanism explains magnesium permeation and selectivity in CorA. *Proceedings of the National Academy of Sciences of the United States of America* **111**, 3002-3007 (2014).
33. O. Dalmas, P. Sompornpisut, F. Bezanilla, E. Perozo, Molecular mechanism of Mg^{2+}-dependent gating in CorA. *Nature communications* **5**, 3590 (2014).
34. D. Matthies *et al.*, Cryo-EM Structures of the Magnesium Channel CorA Reveal Symmetry Break upon Gating. *Cell* **164**, 747-756 (2016).
35. T. Kawate, E. Gouaux, Fluorescence-detection size-exclusion chromatography for precrystallization screening of integral membrane proteins. *Structure* **14**, 673-681 (2006).
36. R. Pfoh *et al.*, Structural asymmetry in the magnesium channel CorA points to sequential allosteric regulation. *Proceedings of the National Academy of Sciences of the United States of America* **109**, 18809-18814 (2012).
37. A. Guskov *et al.*, Structural insights into the mechanisms of Mg^{2+} uptake, transport, and gating by CorA. *Proceedings of the National Academy of Sciences of the United States of America* **109**, 18459-18464 (2012).
38. J. Payandeh *et al.*, Probing structure-function relationships and gating mechanisms in the CorA Mg^{2+} transport system. *The Journal of biological chemistry* **283**, 11721-11733 (2008).
39. X. Yang *et al.*, Mutagenesis analysis of GMN motif in Arabidopsis thaliana Mg^{2+} transporter MRS2-1. *Bioscience, Biotechnology, and Biochemistry* **86**, 870-874 (2022).
40. J. Payandeh, T. Scheuer, N. Zheng, W. A. Catterall, The crystal structure of a voltage-gated sodium channel. *Nature* **475**, 353-358 (2011).

41. X. Zhang *et al.*, Crystal structure of an orthologue of the NaChBac voltage-gated sodium channel. *Nature* **486**, 130-134 (2012).
42. S. G. Brohawn, E. B. Campbell, R. MacKinnon, Physical mechanism for gating and mechanosensitivity of the human TRAAK K^+ channel. *Nature* **516**, 126-130 (2014).
43. H. Yang *et al.*, Pore architecture of TRIC channels and insights into their gating mechanism. *Nature* 10.1038/nature19767 (2016).
44. G. Kasuya *et al.*, Crystal structures of the TRIC trimeric intracellular cation channel orthologues. *Cell research* **26**, 1288-1301 (2016).
45. M. Hattori, Y. Tanaka, S. Fukai, R. Ishitani, O. Nureki, Crystal structure of the MgtE Mg^{2+} transporter. *Nature* **448**, 1072-1075 (2007).
46. M. Hattori *et al.*, Mg^{2+}-dependent gating of bacterial MgtE channel underlies Mg^{2+} homeostasis. *The EMBO journal* **28**, 3602-3612 (2009).
47. F. Jin *et al.*, The structure of MgtE in the absence of magnesium provides new insights into channel gating. *PLoS biology* **19**, e3001231 (2021).
48. S. J. Conn *et al.*, Magnesium transporters, MGT2/MRS2-1 and MGT3/MRS2-5, are important for magnesium partitioning within Arabidopsis thaliana mesophyll vacuoles. *New Phytol* **190**, 583-594 (2011).
49. R. J. Tang *et al.*, Tonoplast CBL-CIPK calcium signaling network regulates magnesium homeostasis in Arabidopsis. *Proc Natl Acad Sci U S A* **112**, 3134-3139 (2015).
50. S. I. Inoue *et al.*, A tonoplast-localized magnesium transporter is crucial for stomatal opening in Arabidopsis under high Mg^{2+} conditions. *New Phytol* **236**, 864-877 (2022).
51. T. Saito *et al.*, Expression and functional analysis of the CorA-MRS2-ALR-type magnesium transporter family in rice. *Plant Cell Physiol* **54**, 1673-1683 (2013).
52. H. Li *et al.*, Identification, and Functional and Expression Analyses of the CorA/MRS2/MGT-Type Magnesium Transporter Family in Maize. *Plant Cell Physiol* **57**, 1153-1168 (2016).
53. R. Reddi, K. Matulef, E. Riederer, P. Moenne-Loccoz, F. I. Valiyaveetil, Structures of Gating Intermediates in a K^+ channel. *J Mol Biol* **433**, 167296 (2021).
54. N. Bharambe *et al.*, Cryo-EM structures of prokaryotic ligand-gated ion channel GLIC provide insights into gating in a lipid environment. *Nat Commun* **15**, 2967 (2024).
55. J. Yu *et al.*, Mechanism of gating and partial agonist action in the glycine receptor. *Cell* **184**, 957-968 e921 (2021).
56. S. K. Erramilli *et al.*, Conformational ensembles of the magnesium channel CorA reveal structural basis for channel gating. *Proc Natl Acad Sci U S A* **123**, e2512532123 (2026).
57. D. J. Scott *et al.*, A Novel Ultra-Stable, Monomeric Green Fluorescent Protein For Direct Volumetric Imaging of Whole Organs Using CLARITY. *Sci Rep* **8**, 667 (2018).
58. A. Punjani, J. L. Rubinstein, D. J. Fleet, M. A. Brubaker, cryoSPARC: algorithms for rapid unsupervised cryo-EM structure determination. *Nat Methods* **14**, 290-296 (2017).
59. A. Punjani, H. Zhang, D. J. Fleet, Non-uniform refinement: adaptive regularization improves single-particle cryo-EM reconstruction. *Nat Methods* **17**, 1214-1221 (2020).
60. A. Punjani, D. J. Fleet, 3D variability analysis: Resolving continuous flexibility and discrete heterogeneity from single particle cryo-EM. *J Struct Biol* **213**, 107702 (2021).
61. M. Mirdita *et al.*, ColabFold: making protein folding accessible to all. *Nature Methods* **19**, 679-682 (2022).
62. J. Jumper *et al.*, Highly accurate protein structure prediction with AlphaFold. *Nature* **596**, 583-

589 (2021).

63. D. Liebschner *et al.*, Macromolecular structure determination using X-rays, neutrons and electrons: recent developments in Phenix. *Acta Crystallographica Section D* **75**, 861-877 (2019).

64. P. Emsley, K. Cowtan, Coot: model-building tools for molecular graphics. *Acta Crystallographica Section D: Biological Crystallography* **60**, 2126-2132 (2004).

65. E. F. Pettersen *et al.*, UCSF Chimera--a visualization system for exploratory research and analysis. *Journal of computational chemistry* **25**, 1605-1612 (2004).

66. F. Sievers, D. G. Higgins, Clustal Omega, accurate alignment of very large numbers of sequences. *Methods Mol Biol* **1079**, 105-116 (2014).

67. X. Robert, C. Guillon, P. Gouet, FoldScript: a web server for the efficient analysis of AI-generated 3D protein models. *Nucleic acids research* **53**, W277-W282 (2025).

68. O. S. Smart, J. G. Neduvelil, X. Wang, B. A. Wallace, M. S. Sansom, HOLE: a program for the analysis of the pore dimensions of ion channel structural models. *J Mol Graph* **14**, 354-360, 376 (1996).

69. M. Y. Sun *et al.*, Mechanism of capsaicin entry into buried vanilloid sites in TRPV1. *Nat Chem Biol* **21**, 1957-1969 (2025).

70. E. Schmidt *et al.*, Structural mechanism of TRPM7 channel regulation by intracellular magnesium. *Cell Mol Life Sci* **79**, 225 (2022).

71. Y. Z. Huang *et al.*, TRPV1 analgesics disturb core body temperature via a biased allosteric mechanism involving conformations distinct from that for nociception. *Neuron* **112**, 1815-1831 e1814 (2024).

72. Y. Y. Lin *et al.*, Finely ordered intracellular domain harbors an allosteric site to modulate physiopathological function of P2X3 receptors. *Nat Commun* **15**, 7652 (2024).

73. X. F. Ma *et al.*, The long beta2,3-sheets encoded by redundant sequences play an integral role in the channel function of P2X7 receptors. *J Biol Chem* **298**, 102002 (2022).

74. A. Sali, T. L. Blundell, Comparative protein modelling by satisfaction of spatial restraints. *J Mol Biol* **234**, 779-815 (1993).

75. A. Sali, J. P. Overington, Derivation of rules for comparative protein modeling from a database of protein structure alignments. *Protein Sci* **3**, 1582-1596 (1994).

76. M. H. Olsson, C. R. Sondergaard, M. Rostkowski, J. H. Jensen, PROPKA3: Consistent Treatment of Internal and Surface Residues in Empirical pKa Predictions. *J Chem Theory Comput* **7**, 525-537 (2011).

77. J. Lee *et al.*, CHARMM-GUI Input Generator for NAMD, GROMACS, AMBER, OpenMM, and CHARMM/OpenMM Simulations Using the CHARMM36 Additive Force Field. *J Chem Theory Comput* **12**, 405-413 (2016).

78. M. A. Lomize, A. L. Lomize, I. D. Pogozheva, H. I. Mosberg, OPM: orientations of proteins in membranes database. *Bioinformatics* **22**, 623-625 (2006).

79. W. L. Jorgensen, J. Chandrasekhar, J. D. Madura, R. W. Impey, M. L. Klein, Comparison of simple potential functions for simulating liquid water. *The Journal of Chemical Physics* **79**, 926-935 (1983).

80. M. J. Abraham *et al.*, GROMACS: High performance molecular simulations through multi-level parallelism from laptops to supercomputers. *SoftwareX* **1-2**, 19-25 (2015).

81. A. D. MacKerell *et al.*, All-atom empirical potential for molecular modeling and dynamics studies of proteins. *J Phys Chem B* **102**, 3586-3616 (1998).

905 82. S. Nosé, A molecular dynamics method for simulations in the canonical ensemble. *Molecular*
906 *Physics* **52**, 255-268 (1984).
907 83. W. G. Hoover, Canonical dynamics: Equilibrium phase-space distributions. *Phys Rev A Gen*
908 *Phys* **31**, 1695-1697 (1985).
909 84. M. Parrinello, A. Rahman, Polymorphic transitions in single crystals: A new molecular
910 dynamics method. *Journal of Applied Physics* **52**, 7182-7190 (1981).
911 85. B. Hess, H. Bekker, H. J. C. Berendsen, J. G. E. M. Fraaije, LINCS: A linear constraint solver
912 for molecular simulations. *Journal of computational chemistry* **18**, 1463-1472 (1997).
913 86. T. Darden, D. York, L. Pedersen, Particle mesh Ewald: An N·log(N) method for Ewald sums in
914 large systems. *The Journal of Chemical Physics* **98**, 10089-10092 (1993).

915

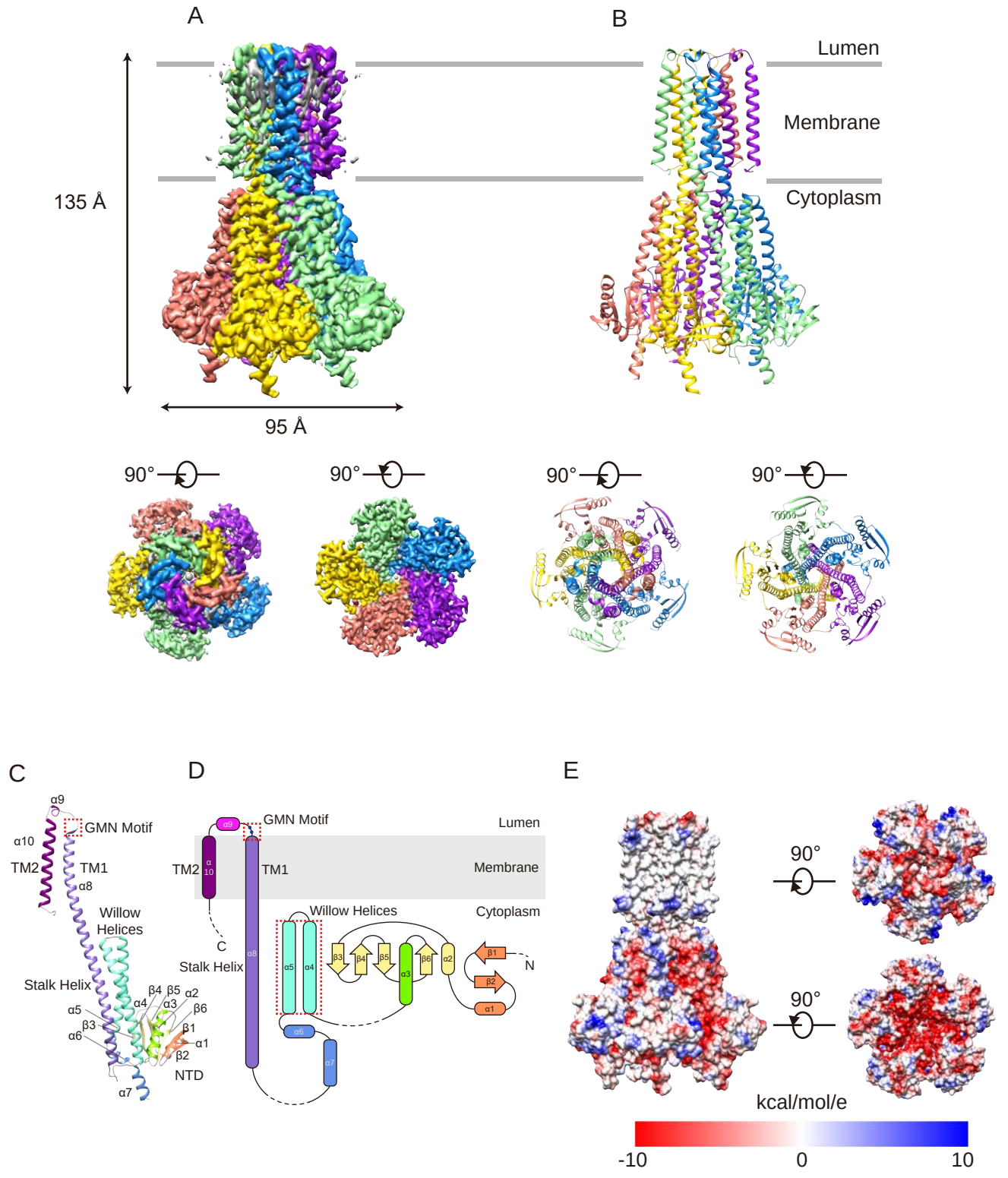
A
B
Lumen
Membrane
Cytoplasm
135 Å
95 Å
90°
90°
90°
90°
C
D
E
α9
GMN Motif
α10
TM2
TM1
α8
Willow
Helices
Stalk Helix
β4 β5 α2
α4 α3 β6
α5 β3 β1
α6 α1
β2
NTD
α7
GMN Motif
Lumen
TM2
α10
TM1
Membrane
Willow Helices
Cytoplasm
C
Stalk Helix
N
90°
90°
kcal/mol/e
-10
0
10

Figure 1

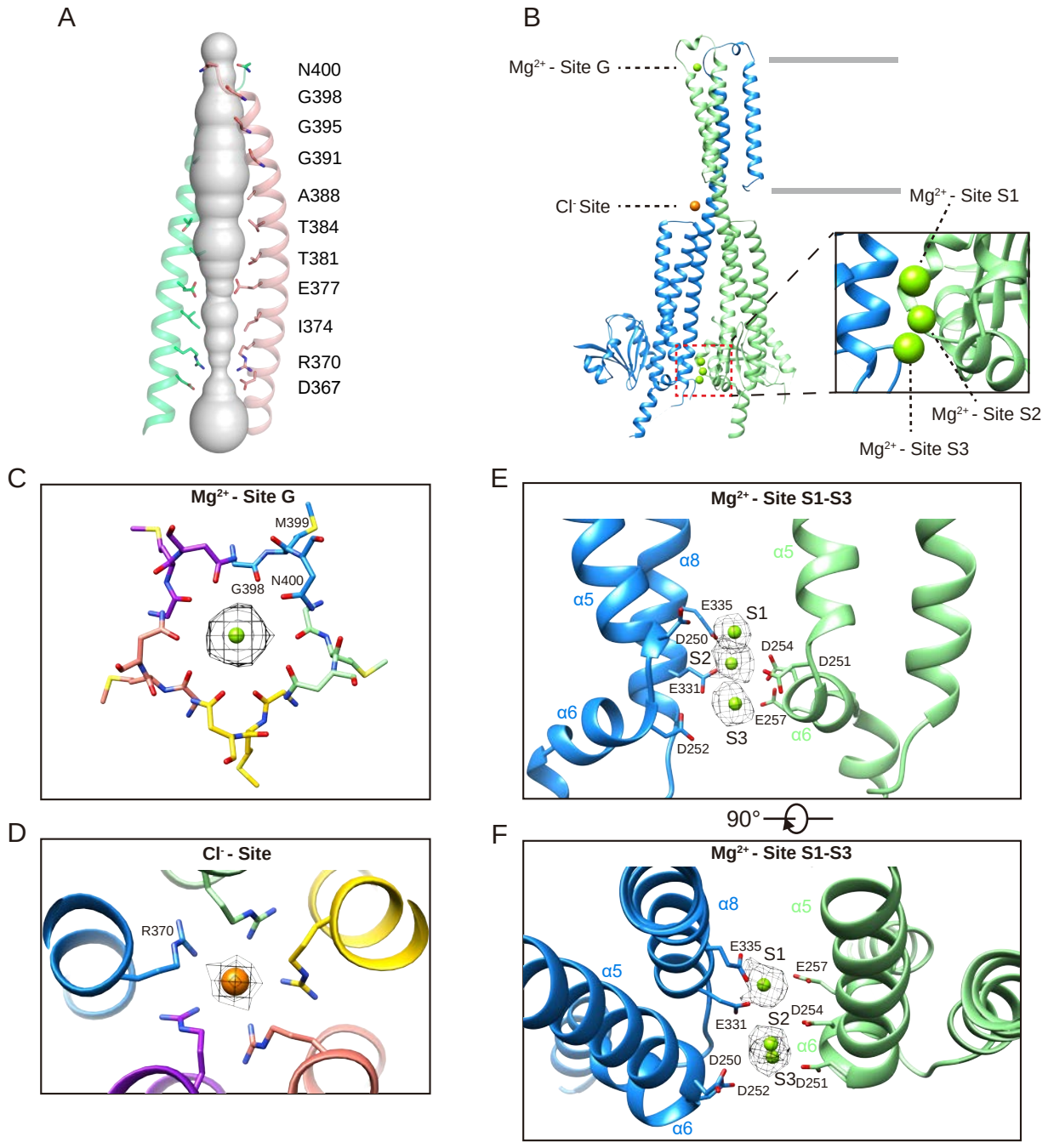
A
N400
G398
G395
G391
A388
T384
T381
E377
I374
R370
D367
B
Mg2+ - Site G
Cl- Site
Mg2+ - Site S1
Mg2+ - Site S2
Mg2+ - Site S3
C
Mg2+ - Site G
M399
G398
N400
D
Cl- - Site
R370
E
Mg2+ - Site S1-S3
α8
α5
E335
S1
D250
S2
D254
D251
E331
E257
α6
S3
D252
90°
F
Mg2+ - Site S1-S3
α8
α5
E335
S1
E257
α5
E331
S2
D254
α6
D250
S3
D251
D252
α6

Figure 2

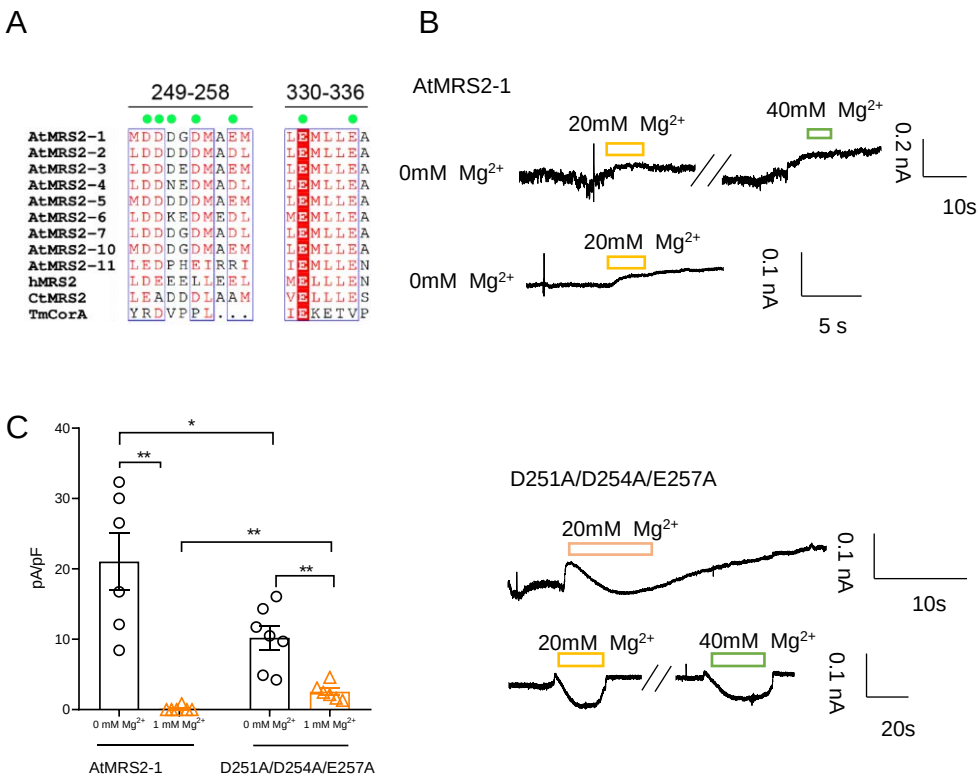
A
249-258
330-336
AtMRS2-1
AtMRS2-2
AtMRS2-3
AtMRS2-4
AtMRS2-5
AtMRS2-6
AtMRS2-7
AtMRS2-10
AtMRS2-11
hMRS2
CtMRS2
TmCorA
B
AtMRS2-1
20mM Mg2+
40mM Mg2+
0mM Mg2+
0.2 nA
10s
20mM Mg2+
0mM Mg2+
0.1 nA
5 s
C
pA/pF
0 mM Mg2+
1 mM Mg2+
AtMRS2-1
D251A/D254A/E257A
D251A/D254A/E257A
20mM Mg2+
0.1 nA
10s
20mM Mg2+
40mM Mg2+
0.1 nA
20s

Figure 3

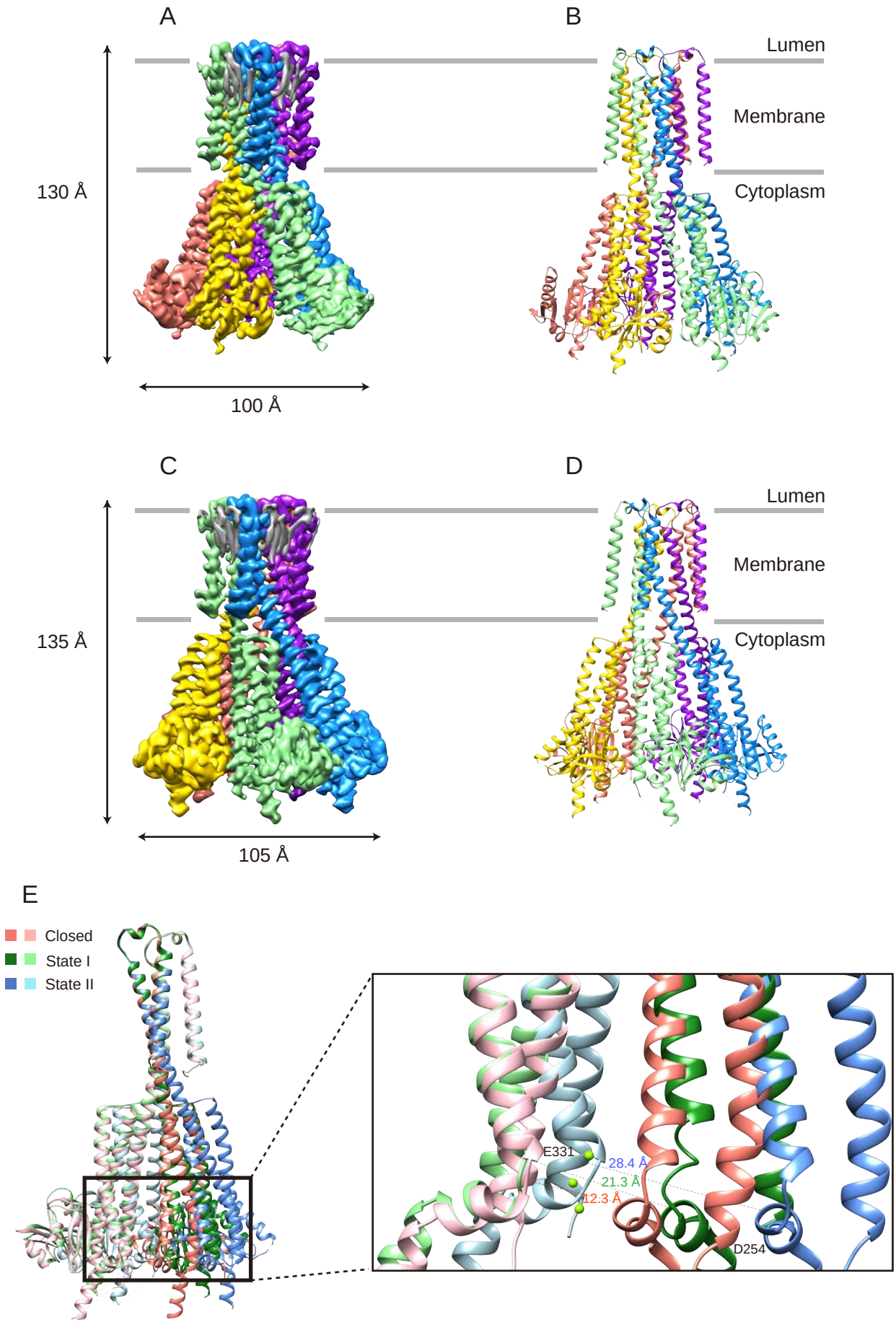
A
B
Lumen
Membrane
Cytoplasm
130 Å
100 Å
C
D
Lumen
Membrane
Cytoplasm
135 Å
105 Å
E
Closed
State I
State II
E331
28.4 Å
21.3 Å
12.3 Å
D254

Figure 4

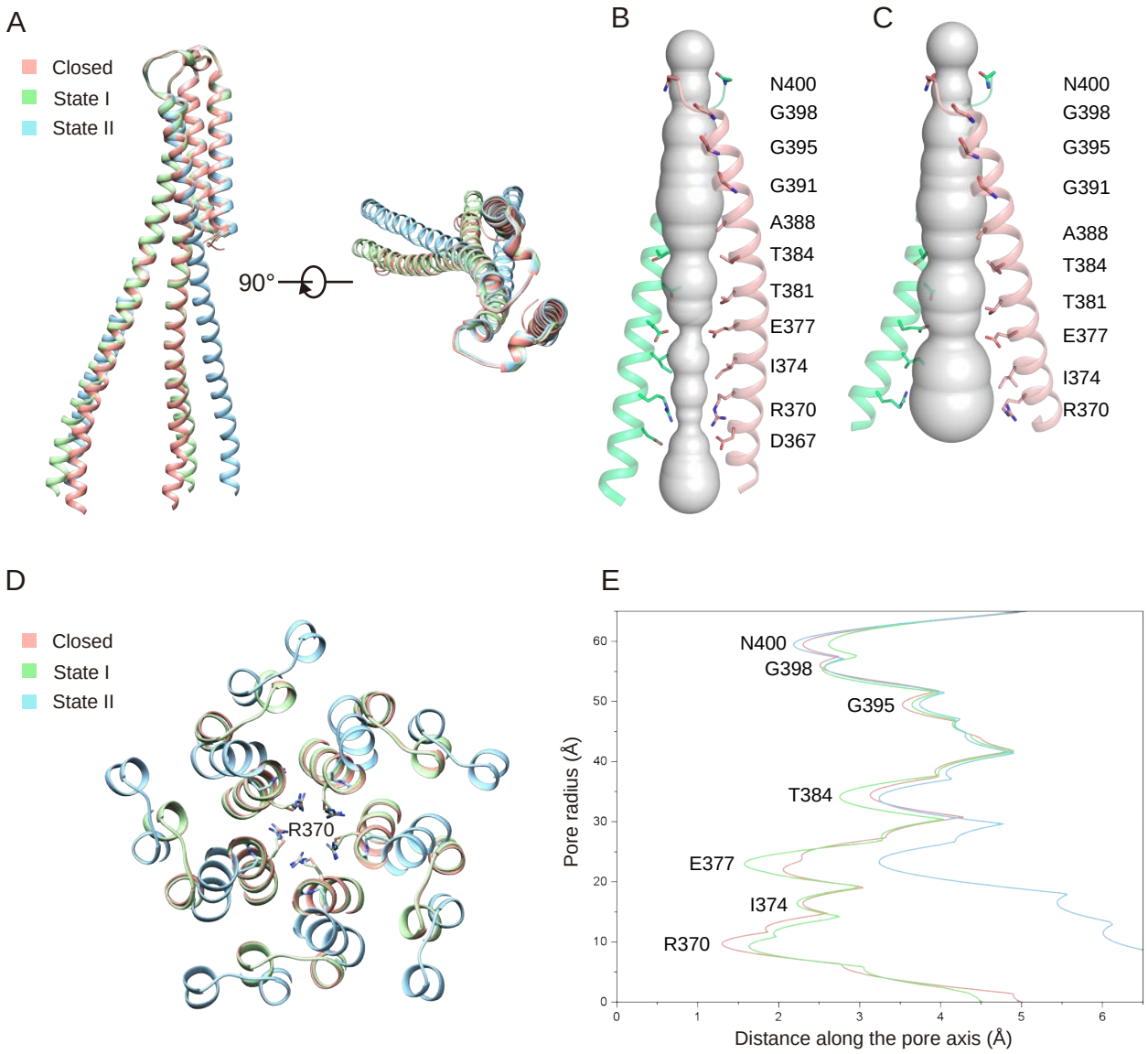

Figure 5

Figure 5

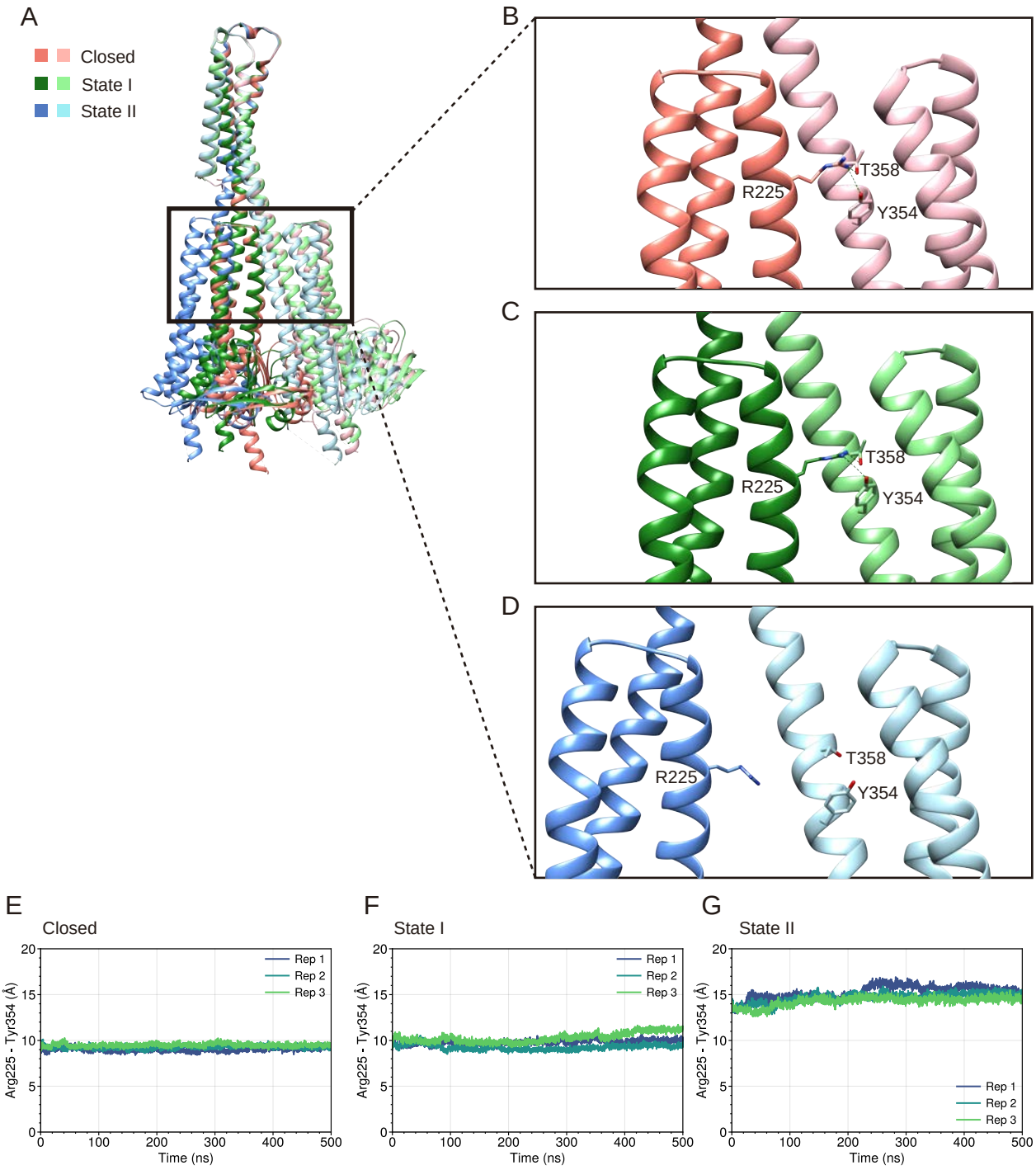
A
Closed
State I
State II
B
T358
R225
Y354
C
T358
R225
Y354
D
R225
T358
Y354
E
Closed
F
State I
G
State II
Arg225 - Tyr354 (Å)
Time (ns)
Rep 1
Rep 2
Rep 3
0
5
10
15
20
0
100
200
300
400
500

Figure 6

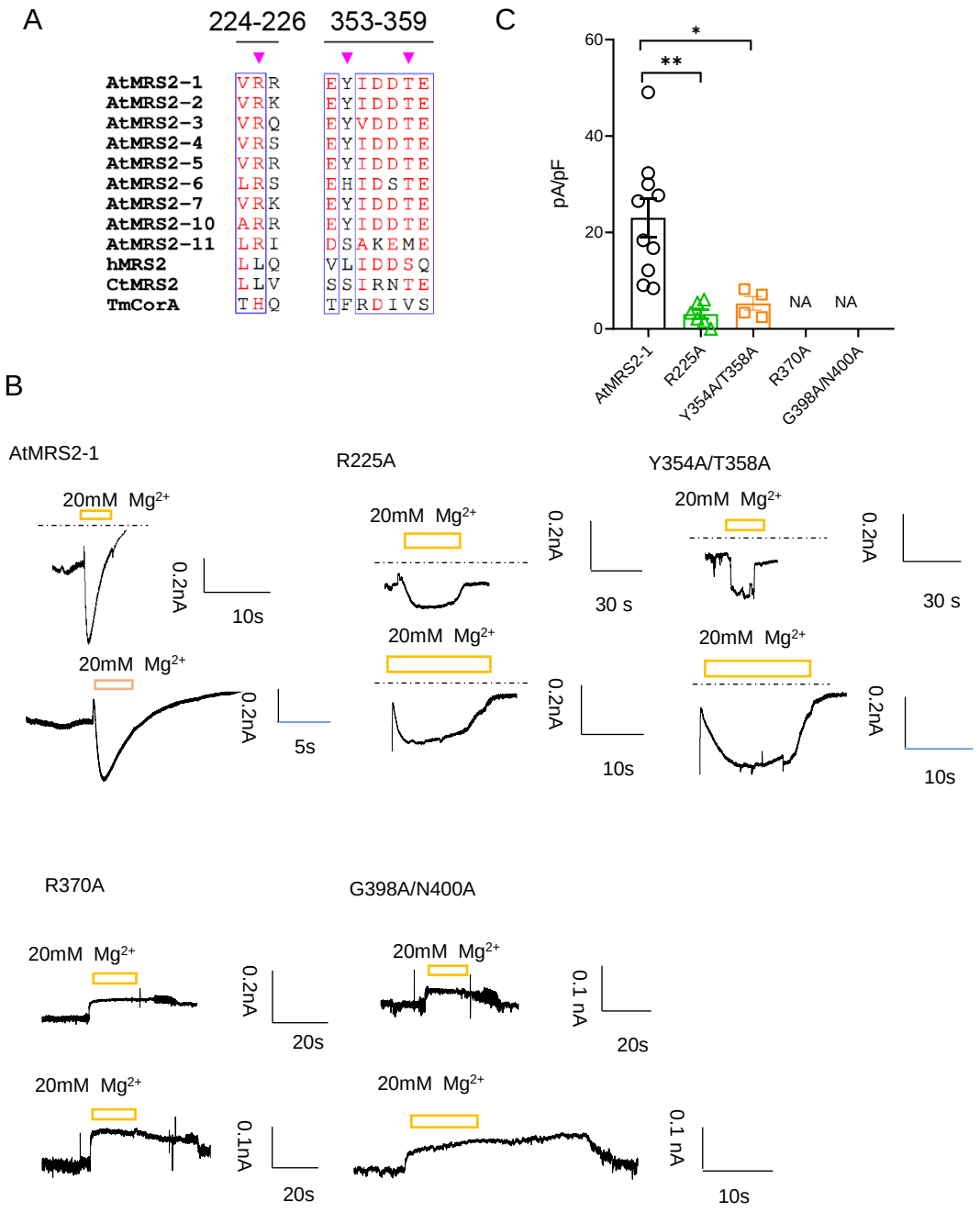
A
224-226
353-359
AtMRS2-1 VRR EYIDDTE
AtMRS2-2 VRK EYIDDTE
AtMRS2-3 VRQ EYVDDTE
AtMRS2-4 VRS EYIDDTE
AtMRS2-5 VRR EYIDDTE
AtMRS2-6 LRS EHIDSTE
AtMRS2-7 VRK EYIDDTE
AtMRS2-10 ARR EYIDDTE
AtMRS2-11 LRI DSAKEME
hMRS2 LLQ VLIDDSQ
CtMRS2 LLV SSIRNTE
TmCorA THQ TFRDIVS
C
pA/pF
60
40
20
0
*
**
NA
NA
AtMRS2-1
R225A
Y354A/T358A
R370A
G398A/N400A
B
AtMRS2-1
20mM Mg2+
0.2nA
10s
20mM Mg2+
0.2nA
5s
R225A
20mM Mg2+
0.2nA
30 s
20mM Mg2+
0.2nA
10s
Y354A/T358A
20mM Mg2+
0.2nA
30 s
20mM Mg2+
0.2nA
10s
R370A
20mM Mg2+
0.2nA
20s
20mM Mg2+
0.1nA
20s
G398A/N400A
20mM Mg2+
0.1 nA
20s
20mM Mg2+
0.1 nA
10s

Figure 7

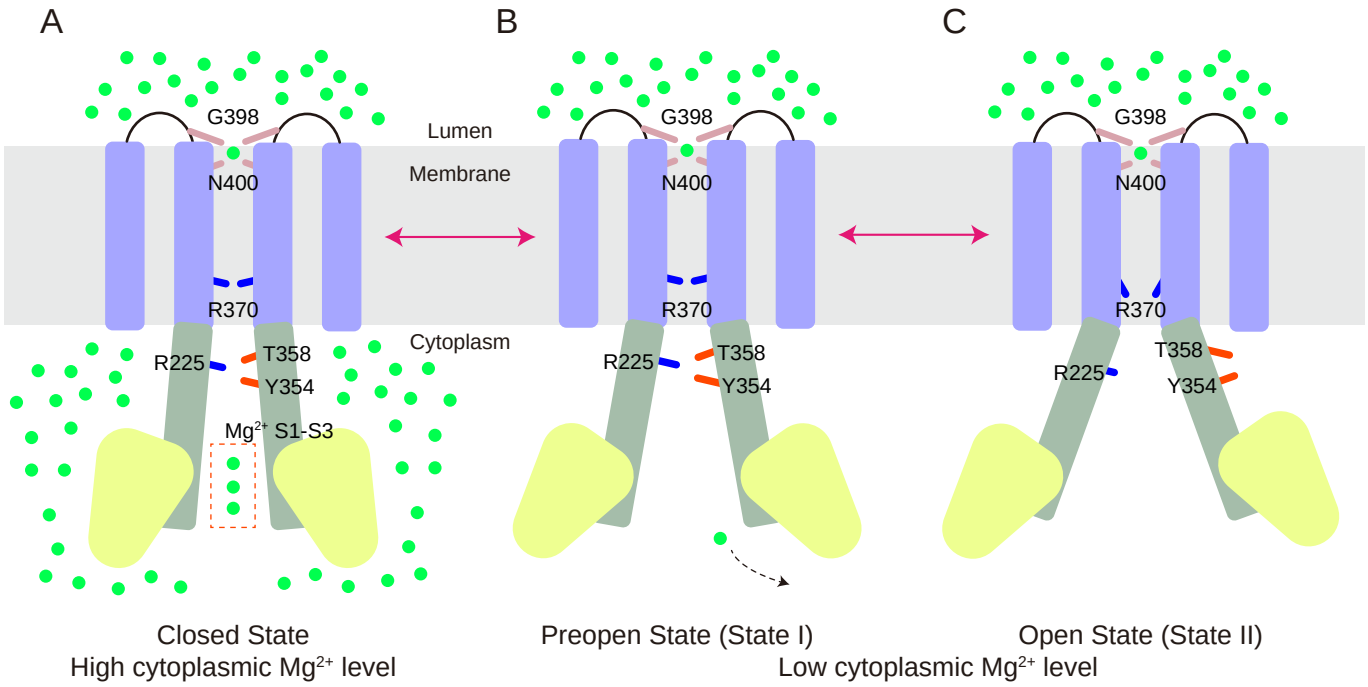
A
B
C
G398
N400
R370
R225
T358
Y354
Lumen
Membrane
Cytoplasm
Mg2+ S1-S3
Closed State
High cytoplasmic Mg2+ level
Preopen State (State I)
Open State (State II)
Low cytoplasmic Mg2+ level

Figure 8